

Absolute OH Number Density Measurements in Lean Fuel-Air Mixtures Excited by a Repetitively Pulsed Nanosecond Discharge

Zhiyao Yin, Campbell D. Carter*, Walter R. Lempert, and Igor V. Adamovich

Michael A. Chaszeyka Nonequilibrium Thermodynamics Laboratories

*Department of Mechanical Engineering,
The Ohio State University, Columbus, OH 43210*

**Air Force Research Laboratory, Dayton, OH 45433*

Abstract

OH Laser Induced Fluorescence (LIF) is used for temperature and absolute OH number density measurements in an atmospheric pressure, near stoichiometric CH₄-air flame generated by a Hencken burner. OH rotational temperature is inferred with excitation scans of both the OH A-X (0,0) and (1,0) bands. OH LIF signal is corrected by considering transition-dependent total radiative decay rate, laser attenuation, and fluorescence trapping. The relative OH concentrations are put on an absolute scale by calibrating the optical collection constant using Rayleigh scattering. The measured absolute OH number density in the flame is compared with laser absorption measurements done at the same locations, showing good agreement and thus demonstrating the efficacy of our calibration approach employing Rayleigh scattering—for a low temperature and pressure, lean, fuel-air mixtures excited by a repetitively pulsed nanosecond (nsec) discharge. Here, a premixed fuel-air flow, initially at T₀=500 K and P=100 torr, is excited by the discharge in a plane-to-plane geometry, operated in burst mode at 10 kHz pulse repetition rate. Burst duration is limited to 50 pulses, to preclude plasma-assisted ignition. The discharge uniformity in air and fuel-air flows is verified using sub-nsec-gated images, employing an intensified charge-coupled device camera. Time-resolved, absolute OH number density, measured after the discharge burst, demonstrates that OH concentration in C₂H₄-air, C₃H₈-air, and CH₄ is highest in the leanest mixtures, while in H₂-air, OH concentration is nearly independent of the equivalence ratio. In C₂H₄-air and C₃H₈-air, unlike in CH₄-air and in H₂-air, transient OH-concentration overshoot after the discharge is detected. In C₂H₄-air and C₃H₈-air, OH decays after the discharge on the time scale of ~0.02-0.1 msec, suggesting little accumulation during the burst of pulses repeated at 10 kHz. In CH₄-air and H₂-air, OH concentration decays within ~0.1-1.0 msec and 0.5-1.0 msec, respectively, showing that it may accumulate during the burst.

The experimental results are compared with kinetic modeling calculations using plasma / fuel chemistry model employing several H₂-air and hydrocarbon-air chemistry mechanisms. Kinetic mechanisms for H₂-air, CH₄-air, and C₂H₄-air developed by A. Konnov provide the best overall agreement with OH measurements. In C₃H₈-air, none of the hydrocarbon chemistry mechanisms agrees well with the data. The results show the need for development of an accurate, predictive low-temperature plasma chemistry / fuel chemistry kinetic model applicable to fuels C₃ and higher.

Report Documentation Page		<i>Form Approved</i> <i>OMB No. 0704-0188</i>	
Public reporting burden for the collection of information is estimated to average 1 hour per response, including the time for reviewing instructions, searching existing data sources, gathering and maintaining the data needed, and completing and reviewing the collection of information. Send comments regarding this burden estimate or any other aspect of this collection of information, including suggestions for reducing this burden, to Washington Headquarters Services, Directorate for Information Operations and Reports, 1215 Jefferson Davis Highway, Suite 1204, Arlington VA 22202-4302. Respondents should be aware that notwithstanding any other provision of law, no person shall be subject to a penalty for failing to comply with a collection of information if it does not display a currently valid OMB control number.			
1. REPORT DATE JAN 2013		2. REPORT TYPE	
		3. DATES COVERED 00-00-2013 to 00-00-2013	
4. TITLE AND SUBTITLE Absolute OH Number Density Measurements in Lean Fuel-Air Mixtures Excited by a Repetitively Pulsed Nanosecond Discharge		5a. CONTRACT NUMBER	
		5b. GRANT NUMBER	
		5c. PROGRAM ELEMENT NUMBER	
6. AUTHOR(S)		5d. PROJECT NUMBER	
		5e. TASK NUMBER	
		5f. WORK UNIT NUMBER	
7. PERFORMING ORGANIZATION NAME(S) AND ADDRESS(ES) Ohio State University, Department of Mechanical and Aerospace Engineering, Michael A. Chaszeyka Nonequilibrium Thermodynamic Laboratories, Columbus, OH, 43210		8. PERFORMING ORGANIZATION REPORT NUMBER	
9. SPONSORING/MONITORING AGENCY NAME(S) AND ADDRESS(ES)		10. SPONSOR/MONITOR'S ACRONYM(S)	
		11. SPONSOR/MONITOR'S REPORT NUMBER(S)	
12. DISTRIBUTION/AVAILABILITY STATEMENT Approved for public release; distribution unlimited			
13. SUPPLEMENTARY NOTES			

14. ABSTRACT

OH Laser Induced Fluorescence (LIF) is used for temperature and absolute OH number density measurements in an atmospheric pressure, near stoichiometric CH₄-air flame generated by a Hencken burner. OH rotational temperature is inferred with excitation scans of both the OH A-X (0,0) and (1,0) bands. OH LIF signal is corrected by considering transition-dependent total radiative decay rate, laser attenuation, and fluorescence trapping. The relative OH concentrations are put on an absolute scale by calibrating the optical collection constant using Rayleigh scattering. The measured absolute OH number density in the flame is compared with laser absorption measurements done at the same locations, showing good agreement and thus demonstrating the efficacy of our calibration approach employing Rayleigh scattering. For a low temperature and pressure, lean, fuel-air mixtures excited by a repetitively pulsed nanosecond (nsec) discharge. Here, a premixed fuel-air flow, initially at T₀=500 K and P=100 torr, is excited by the discharge in a plane-to-plane geometry, operated in burst mode at 10 kHz pulse repetition rate. Burst duration is limited to 50 pulses, to preclude plasma-assisted ignition. The discharge uniformity in air and fuel-air flows is verified using sub-nsec-gated images, employing an intensified charge-coupled device camera. Time-resolved, absolute OH number density, measured after the discharge burst, demonstrates that OH concentration in C₂H₄-air, C₃H₈-air, and CH₄ is highest in the leanest mixtures, while in H₂-air, OH concentration is nearly independent of the equivalence ratio. In C₂H₄-air and C₃H₈-air, unlike in CH₄-air and in H₂-air, transient OH-concentration overshoot after the discharge is detected. In C₂H₄-air and C₃H₈-air, OH decays after the discharge on the time scale of ~0.02-0.1 msec, suggesting little accumulation during the burst of pulses repeated at 10 kHz. In CH₄-air and H₂-air, OH concentration decays within ~0.1-1.0 msec and 0.5-1.0 msec, respectively, showing that it may accumulate during the burst. The experimental results are compared with kinetic modeling calculations using plasma / fuel chemistry model employing several H₂-air and hydrocarbon-air chemistry mechanisms. Kinetic mechanisms for H₂-air, CH₄-air, and C₂H₄-air developed by A. Konnov provide the best overall agreement with OH measurements. In C₃H₈-air, none of the hydrocarbon chemistry mechanisms agrees well with the data. The results show the need for development of an accurate, predictive low-temperature plasma chemistry / fuel chemistry kinetic model applicable to fuels C₃ and higher.

15. SUBJECT TERMS

16. SECURITY CLASSIFICATION OF:

a. REPORT
unclassified

b. ABSTRACT
unclassified

c. THIS PAGE
unclassified

17. LIMITATION OF
ABSTRACT

**Same as
Report (SAR)**

18. NUMBER
OF PAGES

34

19a. NAME OF
RESPONSIBLE PERSON

1. Introduction

In recent years, the kinetic mechanism of nonequilibrium plasmas assisted ignition and combustion has been intensively studied through both experiments and kinetic modeling [1-7]. This research has demonstrated that conventional plasma/combustion chemistry falls short in fully capturing experimentally observed phenomena [7] and that either *i)* new pathways are needed in the combustion mechanism [1, 6] or *ii)* elementary reaction rates of electron impact processes and reactions involving excited species should be re-examined [2]. The consensus is that experimental data in various fuel-oxidizer mixtures at a wide range of pressures and temperatures are needed for developing a truly predictive plasma/combustion chemistry model. At the core of the kinetic study is the accurate quantification of key parameters found in both plasma and combustion processes, such as temperature and radical species concentration. Non-intrusive laser diagnostics is well suited for this task and is capable of providing both spatially and temporally resolved information.

One of the most important intermediate species in combustion systems is the hydroxyl radical (OH). Various techniques for detection of OH radicals via Laser Induced Fluorescence (LIF) have been developed in the last decade. One of the difficulties in OH LIF is converting relative fluorescence signal into absolute number density. This involves proper signal correction, accurate temperature measurement, and calibration for the efficiency of the signal collection system, which usually needs to be tailored for the specific experimental setup. Laser absorption is traditionally used for obtaining a reference point in combustion systems where OH concentration is abundant and is uniformly distributed, and then OH fluorescence obtained in other conditions can be calibrated by comparing to the LIF signal at the reference point. For plasma assisted combustion at low pressures and low temperatures, however, OH concentration is usually quite low (10^{13} to 10^{14} cm⁻³) [4, 8], and spatially nonuniform regions are usually present in discharge filaments and near the electrode edges [9]. Instead of using absorption measurement, an atmospheric pressure flame generated by a Hencken burner (Technologies for Research) has been demonstrated for calibrating OH signal in plasma assisted combustion [4, 8, 10]. The Hencken burner is designed to generate a near-adiabatic, large and uniform equilibrium burned gas region above its surface and is widely regarded as a reliable source for validating laser diagnostics for temperature and species concentration measurement [11-13]. The idea of using the Hencken burner as a calibration source is that by comparing LIF signals obtained in the plasma and in the Hencken flame, with the same laser and collection optical system, one can obtain the OH number density in the plasma based on calculated equilibrium OH concentration in the flame. This approach, however, may introduce significant error in the absolute OH number density in the plasma if *i)* the measurement location in the flame is not at equilibrium, and/or *ii)* it is difficult to guarantee the same optical alignment for the flame and for the discharge in a specific experimental setup, as encountered in our high temperature plasma reactor system [4, 7]. Also, calculation of the quantum yield requires accurate collisional rates, which are scarce at intermediate temperatures (below flame temperature). An alternative approach, the use of

Rayleigh scattering, becomes attractive in cases where it is preferred to have *in-situ* calibration. Rayleigh scattering has been used as a calibration source for OH [14] and CH LIF [15]. It makes possible the use of the same test cell for calibration, and the Rayleigh signal is proportional to the gas number density inside the test cell, in which case one can choose a non-reacting buffer gas (such as N₂ or air).

The objective of the current work is twofold: *i*) measure temperature and OH concentration in a Hencken burner flame and calibrate it with Rayleigh scattering; compare the calibrated OH number density with that from laser absorption measurements, to establish the reliability (uncertainty) of using Rayleigh scattering as a calibration source; *ii*) measure OH concentration in fuel-air mixtures excited by a nanosecond pulse discharge in a high temperature plasma reactor facility and calibrate it with Rayleigh scattering; compare the absolute OH concentration with kinetic modeling results and validate the plasma/combustion kinetic model.

2. Experimental

For OH LIF calibration measurements performed at AFRL, a 25-mm-square Hencken burner was employed (shown in Fig. 1), using a near-stoichiometric mixture (equivalence ratio of ~ 0.95) of CH₄ (99% purity) and air (compressed). The flow rates were metered with Tylan mass flow controllers, and calibrations for the controllers were confirmed using a Bios Drycal piston-type device. This burner had been modified from the standard model by being constructed without the fuel tubes, and accordingly the burner was operated in a premixed mode. At AFRL, for the combined OH LIF and absorption, an injection seeded Nd:YAG laser (Spectra Physics GCR-170) pumped a tunable dye laser (Lumonics Hyperdye 300). The dye laser output (near 619 nm) was frequency doubled within an Inrad Autotracker III; the UV beam was separated from the dye beam within an Inrad Prism Harmonic Separator (PHS), attenuated to

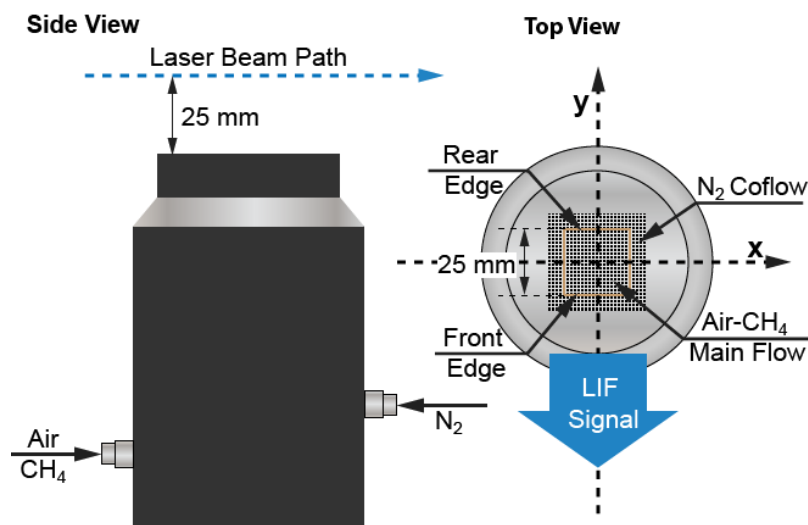


Figure 1: Schematic diagram of the Hencken burner used for OH LIF and laser absorption measurements

about 1 $\mu\text{J}/\text{pulse}$, softly focused over the flame using a lens with a focal length of $f=1$ m, and scanned across transitions in the $A^2\Sigma^+-X^2\Pi$ ($v'=0$, $v''=0$) band. Linewidth for the 309-nm beam was ~ 0.2 cm^{-1} . Beam energies before and after the flame were recorded using Molelectron Joulemeters coupled to integrating spheres; the purpose of the integrating sphere is to remove all spatial information from the beam (before being sampled by the Joulemeter). A simple fused silica window used to reflect a portion of the laser beam to the entrance of the *reference* detector. Joulemeter signals were recorded using a digital oscilloscope (LeCroy Waverunner HRO 64Zi with 12-bit resolution) using a correlated double sampling approach, and relative noise levels between the two signals were as small as 0.03% (though typically $\sim 0.05\%$ for the absorption measurements). OH LIF was imaged synchronously with absorption using a PI-MAX intensified charge coupled device (ICCD) camera having a *Superblue* photocathode; the intensifier gate signal provided the oscilloscope trigger pulse. The purpose of the LIF measurement was to derive the absorption path length (with each absorption measurement):

$$L_{abs}(x=a) = \frac{1}{S_f(x=a)} \int_{-W}^W S_f(x) dx \quad . \quad (1)$$

In Eq. (1), $S_f(x)$ is the LIF signal at location x , a is the calibration location, and the integration limits W were chosen to encompass the entire OH profile. For these measurements, the calibration location is the center of the burner, about 12 mm from the burner edge. Since the profile should represent the OH number density (from a specific rotational ground state), main branch transitions could not be used, due to absorption (and the corresponding distortion of the OH profile). Thus, satellite transitions, which suffer minimal distortion from absorption, were employed. It should be noted that the path length varies slightly as a function of probed ground state.

At OSU, OH concentration and rotational temperature were measured by OH LIF in the near stoichiometric CH_4 -air flame with the same Hencken burner (shown in Fig. 1) and flow control system as used for the absorption and fluorescence trapping measurements at AFRL. LIF was performed with both OH A-X ($v'=0$, $v''=0$) and ($v'=1$, $v''=0$) excitation schemes. The laser system is similar to that at AFRL. An Nd:YAG (Continuum, Model Powerlite 8010) was used to pump a tunable dye laser (Laser Analytical Systems, Model LDL 20505), the output of which was frequency doubled and separated from the fundamental using an Inrad Autotracker II and a PHS. The UV beam was focused into the burnt-gas region with an $f=550$ mm lens. The LIF signal sampling volume was about 100 mm away from the laser focal point, to avoid transition saturation. The laser energy was measured by a power meter (Model P09, Scientech) and monitored during the experiment by a photodiode (Model DET210, Thorlabs). To ensure operation in the linear excitation regime, the laser energy was attenuated down to <0.5 $\mu\text{J}/\text{pulse}$ for ($v'=0$, $v''=0$) excitation and <5 $\mu\text{J}/\text{pulse}$ for ($v'=1$, $v''=0$) excitation, by a combination of a half wave plate and a thin film polarizer. LIF was collected by a 60-mm-long, right angle prism and $f=300$ mm and $f=100$ mm fused silica lenses in sequence to simulate the limited optical access condition encountered in the high temperature plasma reactor (see Fig. 2). The fluorescence was filtered by UG11 Schott glass and attenuated by a quartz neutral density filter ($\text{OD}=0.4$,

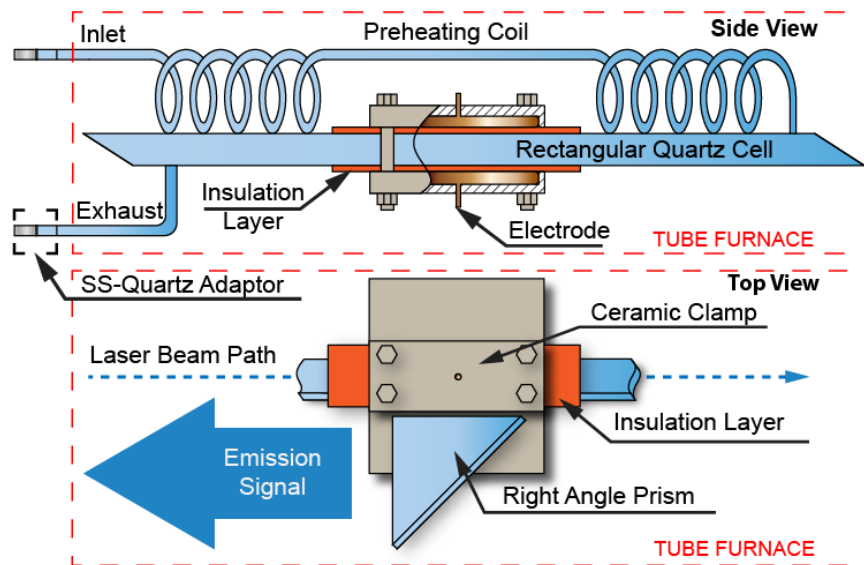


Figure 2: Schematic diagram of the preheated plasma assisted ignition test cell

Newport) before it was directed into a photomultiplier tube (PMT). An entrance slit on the PMT housing was used to limit the sampling volume to be about a 3-mm-long region (from $x=-1.5$ mm to $x=1.5$ mm as shown in Fig. 1) at the center of the laser beam path across the burner. The entire LIF pulse was integrated and analyzed in real time during the experiment using a programmable digital oscilloscope with 1-GHz bandwidth (LeCroy, WAVEPRO 7100A). In order to obtain absolute OH number density from the relative LIF signal taken in the flame, the Rayleigh scattering signal from a “T” shaped cylindrical calibration quartz cell (with CaF_2 Brewster windows for beam entrance and exit, and a CaF_2 optical window on the cross arm for signal collection) was used to calibrate the optical collection efficiency of the LIF system. For that, the laser line was tuned to 308 nm and the calibration cell was supported right above the Hencken burner, to guarantee the same optical alignment as in LIF measurements. Note that a vertically polarized laser beam was used for both LIF and Rayleigh scattering. It is assumed that polarization has negligible effect on the LIF measurements [16], due to broad-band detection. In the present work, both laser absorption and LIF were measured at two probing locations: the laser beam was directed across *i*) the center of the burner ($y=0$ mm) and *ii*) 5-mm inward from the front edge ($y=-7$ mm, as shown in Fig. 1); in both cases the laser beam was 25 mm above the burner surface.

For OH LIF measurements in low pressure plasmas, the experimental setup (shown in Fig. 2) is similar to the one used in our previous studies [4, 7]. The discharge cell / plasma flow reactor consists of a 280-mm-long, 22 mm x 10 mm rectangular cross section quartz channel with wall thickness of 1.75 mm. Two plane quartz windows are fused to the ends of the channel at Brewster angle (for ~ 308 nm), providing optical access in the axial direction. A 60-mm-long, right-angle fused silica prism is placed along the channel to provide optical access from the side. The entire assembly is heated in a tube furnace (Thermcraft, Ltd., with 152-mm-diameter, 254-mm-long heated section), to improve plasma stability. A 1-m-long quartz tube coil inlet preheats

the fuel-air flow to the furnace temperature, which was verified by thermocouple measurements. Two 6-mm-diameter quartz-to-stainless-steel adaptors connect the reactor to the gas delivery system. Two 14 mm x 60 mm rectangular plate copper electrodes, rounded at the edges, are placed on the top and bottom of the quartz channel, as shown in Fig. 1, and held in place by ceramic clamps. A 1.6-mm-thick high-temperature perfluoroelastomer sheet (Kalrez, DuPont) is placed between each electrode and the channel wall, to reduce air gaps and prevent corona discharge outside the cell. In the present work, the electrodes were connected to an FID GmbH FPG 60-100MC4 pulse generator (peak voltage up to 30 kV, pulse duration of 5 nsec, repetition rate up to 100 kHz). The pulser was operated in repetitive burst mode, producing bursts of 50 pulses at a pulse repetition rate of 10 kHz and burst repetition rate of 5 Hz. For laser diagnostics, while the flash lamp of the YAG laser was operated at 10 Hz, Q-switching controlling the laser output was maintained at 5 Hz, to match the burst repetition rate of the pulser and probe OH after each discharge burst.

OH concentration was measured on the channel centerline (about 3-mm-long region) by exciting the $R_1(4,5)$ transition (line assignment notation follows that in Ref. [17]) in the OH A-X (0,0) band in lean CH_4 -, C_2H_4 -, C_3H_8 -, and H_2 -air mixtures, each at two different equivalence ratios. The purity of the fuels is as follows: 99% for CH_4 and C_2H_4 , 99.5% for C_3H_8 , and 99.999% for H_2 . The compressed air cylinder used is Ultra Zero Grade, with 19.9-21.9% of O_2 and <2 ppm H_2O . Fuel and air flow rates through the reactor were metered by MKS mass flow controllers ($<0.4\%$ error at the experimental flow rates, according to the manufacturer's specifications). Fuel and air flows are premixed before entering the cell. The flow velocity through the reactor is estimated to be $u \approx 40$ cm/sec, which is chosen so that the flow barely moves during one burst ($\Delta t = 5$ msec) but refreshes the discharge volume (~ 60 mm) between successive discharge bursts ($\Delta t = 200$ msec). The low flow velocity also improves flow preheating in the inlet coil and reduces pressure drop across the reactor. Absolute OH concentration is obtained by calibrating the relative OH LIF against Rayleigh scattering collected inside the same test cell at 308 nm. For the specific plasma reactor used in this work, this calibration technique requires no change in optical alignment, therefore mitigating uncertainties encountered with the use of an atmospheric-pressure Hencken burner flame [4, 7]. By comparing with the known OH concentration taken with (0,0) excitation, relative OH signal taken with (1,0) excitation from our previous work (Ref. [7]) can also be put on an absolute scale. The details of OH LIF and calibration technique used in this work are discussed in Section 4.

3. OH Laser Absorption

The total absorbance can be calculated from Beer's Law:

$$\begin{aligned}
Abs &= \int_{-\Delta\nu}^{+\Delta\nu} 1 - Tr_\nu d\nu \\
&= \int_{-\Delta\nu}^{+\Delta\nu} 1 - \exp \left[-h\nu_0 \int_0^{L_{abs}} g_a(\nu, \nu_0, T, P) f_B n_{OH} b_{lu} dx \right] d\nu
\end{aligned} \quad (2)$$

In Eq. (2), Tr_ν is the spectral transmittance; h is the Plank constant; ν is the frequency and ν_0 the transition line center (cm^{-1}); n_{OH} is OH number density (cm^{-3}); f_B is the Boltzmann factor for OH molecules in the absorbing state, calculated using the rotational term energies for $X^2\Pi$ $v=0$ state from Coxon [18]; $b_{lu}=B_{lu}/c$ is the Einstein absorption coefficient ($\text{cm}^2\text{J}^{-1}\text{cm}^{-1}$), taken from LIFBASE [19]; g_a is the normalized absorption lineshape and is described by a Voigt function; and L_{abs} is the total absorption path length from Eq. (1). The limits for spectral integration, $\pm\Delta\nu$, it is noted, should include the entire lineshape as nearly as possible. Collisional broadening parameters for calculation of the Voigt function are taken from Rea et al. [20,21], but collisional broadening does not have a major impact on the calculated number density, since the collision widths are much smaller than the Doppler width. n_{OH} is then solved for in an iterative fashion by comparing the calculated and measured total absorbance. The temperature within the Hencken calibration flame is taken to be 2150 K for calculation of the Boltzmann factor and the lineshape parameters.

4. OH LIF and LIF Thermometry

4.1 Basics

When laser excitation rate is low such that the fluorescence scales linearly with the laser energy, the fluorescence signal S_f , can be expressed as follows:

$$S_f(\nu) = n_{OH} f_B b_{lu} E \phi_J g(\nu, \nu_0, \Delta\nu_L, T, P) l \frac{\Omega}{4\pi} \beta \quad (3)$$

In Eq. (3), E is the laser pulse energy (J); ϕ_J is the fluorescence quantum efficiency (or quantum yield); l is the path length sampled by the collection optics (cm); Ω is the solid angle of detection (sr); and β represents the overall conversion coefficient, which consists of the efficiency of the collection optics and response of the detection system; $g(\nu, \nu_0, \Delta\nu_L, T, P)$ is the normalized overlap integral ($1/\text{cm}^{-1}$), in which ν_0 is the center of the transition (cm^{-1}), $\Delta\nu_L$ is the *full width at half maximum* (FWHM) of the laser lineshape, and T and P are pressure and temperature, respectively. The overlap integral is calculated from the product of normalized laser lineshape $g_L(\nu, \Delta\nu_L)$ and the absorption lineshape $g_a(\nu, \nu_0, T, P)$, and has the following form as a function of the laser frequency:

$$g(\nu, \nu_0, \Delta\nu_L, T, P) = \int_{-\Delta\nu}^{+\Delta\nu} g_a(\nu^*, \nu_0, T, P) \cdot g_L(\nu^* - \nu, \Delta\nu_L) d\nu^* . \quad (4)$$

The absorption lineshape is a convolution of Doppler broadening (a function of T and ν_0) and collisional broadening (a function of T and P) lineshapes, i.e., a Voigt lineshape. Without knowing the laser lineshape and its FWHM accurately, evaluation of Eq. (4) may result in significant uncertainty. By performing the excitation scan over an isolated transition, and integrating the fluorescence signal over a wide spectral range, the dependence on the overlap integral is removed (as it integrates to 1, by definition). Eq. (3) then becomes independent of the lineshape and linewidth of laser source and can be rewritten as

$$S_f = n_{OH} f_B b_{lu} E \phi_J l \frac{\Omega}{4\pi} \beta . \quad (5)$$

In the present work, the laser is scanned across multiple transitions in the OH A-X (0,0) and (1,0) bands for the purpose of LIF thermometry in the Hencken flame. In order to separate transitions that are blended due to broad laser linewidth (as encountered at OSU, $\Delta\nu_L$ estimated to be about 0.75 cm^{-1} in the UV, from absorption measurement) and properly integrate each transition, the experimental spectrum is least-squares fitted to a Voigt function, which can be described as a linear combination of multiple Voigt lineshapes:

$$S_{Voigt} = \sum_i c_i f_{B,i}(T) b_{lu,i} g_i(\nu + \Delta\nu_i, \nu_i, \Delta\nu_L, T, P) . \quad (6)$$

In Eq. (6), i represent the i -th transition in the experimental spectrum, $\Delta\nu_i$ is the interval between transition centers (usually a certain transition is used as a reference zero point), c_i accounts for laser energy, quantum yield and optical collection constant as shown in Eq. (5), and spectroscopic values are taken from LIFBASE [19]. By using fitted parameters, each transition ($S_{Voigt,i}$) can be integrated separately (from -10 cm^{-1} to 10 cm^{-1} across linecenter in the present work). Note that this also guarantees same integration range for different transitions, regardless how much they are blended with neighboring transitions.

For inferring rotational temperature (assumed in equilibrium with translational temperature) of the OH ground state, spectrally integrated LIF spectra from different transitions are fitted to a Boltzmann expression, by manipulating Eq. (5):

$$\ln\left(\frac{S_f}{\phi_J b_{lu} g_J}\right) = -\frac{E_J}{kT} + \text{const} . \quad (7)$$

In Eq. (7), E_J is the rotational term energy of lower rotational level J'' taken from Coxon [18]; g_J is the degeneracy of the J'' level (i.e., $2J''+1$). It is important to note that in the present work, quantum yield ϕ_J is considered rotational-level dependent and is not necessarily the same for different transitions. Therefore, it is not included in the *const* term in Eq. (7). For a similar reason, while the least-squares Voigt fit program can be used to infer temperature directly, uncertainties in the quantum yield (part of the term c_i in Eq. (6)) as well as laser linewidth $\Delta\nu_L$

will introduce significant error in the inferred temperature. Therefore, in the Voigt fit, temperature, quantum yield, and laser linewidth are treated as free parameters to generate a best fit that has the least residual when comparing to the experimental spectrum. The integrated LIF spectrum is then treated with signal corrections concerning quantum yield and fluorescence trapping, as will be discussed in the following sections.

4.2 LIF Signal Correction I: Rotational-level-dependent Quantum Yield

For OH A-X (1,0) excitation, the quantum yield can be derived by integrating the rate equation over the entire LIF pulse, while also taking into account spontaneous emission (A_I and A_0), electronic quenching (Q_I and Q_0), and vibrational energy transfer (VET) from $v'=1$ to $v'=0$ (V_{10}):

$$\phi_J = \frac{\varepsilon_I A_I + \varepsilon_0 A_0 V_{10} / (A_0 + Q_0)}{V_{10} + A_I + Q_I} . \quad (8)$$

In Eq. (8), ε_0 and ε_I are the respective signal collection efficiencies for emission from $v'=0$ and $v'=1$ of the $A^2\Sigma^+$ state, which account for differences in fluorescence trapping and spectral sensitivity of the detection system for different transitions. In the absence of VET in the (0,0) excitation scheme (assuming no upwards VET from $v'=0$ to $v'=1$), the fluorescence yield is simply

$$\phi_J = \frac{\varepsilon_0 A_0}{A_0 + Q_0} . \quad (9)$$

Because A_0 varies with the excited rotational state, an assumed rotational distribution must be included. The simplest assumption is that fluorescence originates only from the directly pumped state:

$$A_i = \sum_{j=0}^{\infty} A_{i,j} . \quad (10)$$

For example, for $R_2(6.5)$ excitation in the (0,0) band, A_0 is obtained by summing all the individual (j) radiative decay rates $A_{0,j}$ for transitions originated from $v'=0$, $J'=7.5$, that include $P_2(8.5)$, $Q_2(7.5)$, $R_2(6.5)$, $Q_{21}(7.5)$, $P_{21}(8.5)$ and $R_{21}(6.5)$. This assumption is clearly erroneous, since rotational energy transfer (RET) rates generally exceed electronic quenching rates. Alternatively, one might assume that RET rates are so high that a thermalized distribution exists among rotational populations in the directly excited vibrational state.

In the case of (1,0) excitation, due to the complication introduced by VET, we have assumed that the bias VET causes when populating the $v'=0$ state is small and the $v'=0$ state is thermalized, so that the total radiative decay rate can be evaluated by weighing $A_i(J')$ with the Boltzmann fraction of the specific J' level:

$$A'_i = \sum_{J'} f_B(J') \sum_{j=0}^{\infty} A_{i,j}(J') . \quad (11)$$

In Eq. (11), $f_B(J')$ does not take into account vibrational partition function; it is used as a weighing factor, such that the sum is unity. In this work, the rotational term energies for the vibrational levels in the OH $A^2\Sigma^+$ state are taken from Coxon [18]. Quenching and VET rates are calculated based on published data [22], assuming the burnt-gas composition is close to equilibrium.

For the low pressure conditions found in the plasma reactor (about 0.1 atm), the quenching rate is 5-6 times slower than that at room pressure. The assumption that fluorescence comes only from directly excited J' state is unlikely to apply. In the present work, when treating the LIF signal taken from the plasma reactor, the total radiative decay rate is thus calculated from Eq. (11). Since the detailed gas composition in the probing volume is not measured, it is impractical to use cross sections from literature to calculate quenching and VET rates; furthermore, there is a dearth of collisional data at intermediate temperatures (like those in the plasma reactor). Therefore, certain assumptions must be made in order to evaluate the quantum yield term given by Eqs. (8) and (9). For (1,0) excitation, it should be noted that VET acts to redistribute the A-state population (from $v'=1$ to $v'=0$), and Eq. (8) can be simplified with the following two approximations that eliminate the dependence on the VET rate: 1) $A_0 + Q_0 \approx A_I + Q_I$ (which is not unreasonable based on literature quenching rates, see Refs. [16, 22]) and 2) $\varepsilon_0 A_0 \approx \varepsilon_I A_I$ (also not unreasonable, see Ref. [19]). Thus, the quantum yield for (1,0) excitation can be approximated by that for the (0,0) excitation, i.e., Eq. (9). In this work, for LIF in the low pressure discharge cell, the quantum yield is calculated from the measured fluorescence decay time, $\tau = I/(A_0 + Q_0)$. The quantum yield estimate for (1,0) excitation will be compared with measurements using A-X(0,0) excitation in the discussion section.

4.3 LIF Signal Correction II: Laser Beam Absorption

The overlap integral given by Eq. (4) is derived based on the assumption that the absorbing medium is optically thin. In the atmospheric pressure flame, high OH concentration ($\sim 10^{16} \text{ cm}^{-3}$) can cause considerable laser absorption. This effect can be accounted for by implementing Beer's Law in the expression of the overlap integral, to calculate a modified overlap integral that accounts for the distortion of the laser lineshape (due to absorption) prior to reaching the probe volume:

$$g'(\nu, \nu_0, \Delta\nu_L, T, P, L) = \int_{-\Delta\nu}^{+\Delta\nu} g_a(\nu^*, \nu_0, T, P) \cdot Tr_\nu(\nu^*, \nu_{0,j}, T, P, L) g_L(\nu^* - \nu_L, \Delta\nu_L) d\nu^* . \quad (12)$$

Due to the effect of laser absorption, $\int_{-\Delta\nu}^{+\Delta\nu} g' d\nu$ is less than one. Furthermore, since the LIF sampling volume is not small enough to be treated as a point, the absorption correction needs to be averaged over the laser path sampled by the PMT (in this work, over a 3-mm region). The LIF spectrum is then divided by the ratio of g'/g before the Voigt fit.

4.4 LIF Signal Correction III: Fluorescence Trapping

In the atmospheric pressure flame, OH fluorescence can experience considerable trapping along the signal collection path. Similar assumptions used for evaluating the total radiative decay rate can be applied here for estimating the trapping ratio. In cases where only emission from the directly excited J' state is considered, the total fluorescence transmittance due to trapping is a sum of transmittances of individual transitions, weighted by their Einstein A coefficients:

$$TR_i = \frac{\sum_{j=0}^{\infty} A_{i,j} TL_{i,j}}{\sum_{j=0}^{\infty} A_{i,j}} . \quad (13)$$

where TR_i is the total fluorescence transmittance for vibrational level $v'=i$ in the excited electronic state. $TL_{i,j}$ is the LIF transmittance from the j -th transition and is calculated by assuming g_a as the emission manifold, i.e.:

$$TL_{i,j} = \int_{-\Delta\nu}^{+\Delta\nu} Tr_v(\nu^*, \nu_{0,j}, T, P, L) \cdot g_a(\nu^*, \nu_{0,j}, T, P) d\nu^* . \quad (14)$$

When the thermalization assumption is applied, emission from a certain J' level is further weighted by its Boltzmann fraction, as in:

$$TR'_i = \sum_{J'} f_B(J') \frac{\sum_{j=0}^{\infty} A_{i,j}(J') TL_{i,j}(J')}{\sum_{j=0}^{\infty} A_{i,j}(J')} . \quad (15)$$

Different trapping analyses can be assessed by comparing to trapping measurements done at AFRL, as noted in Section 2.

5. Rayleigh Scattering Calibration

In order to calculate the absolute OH concentration on from Eq. (5), the product of l , Ω , and β (all related to the optical collection system) is needed and can be determined from Rayleigh scattering as follows:

$$S_{Rayleigh} = \frac{\varepsilon_R}{hc \nu_L} \left(\frac{\partial \sigma}{\partial \Omega} \right) l \Omega \beta \cdot (NE) . \quad (16)$$

In Eq. (16), ε_R is the collection efficiency of the Rayleigh scattering; $N=P/kT$ is the gas number density (cm^{-3}); and E is the pulse energy used for the Rayleigh scattering measurements. For vertically polarized excitation, while collecting both polarization components, the differential cross section (cm^2/sr) in terms of index of refraction (n_0) is given by:

$$\frac{\partial \sigma}{\partial \Omega} = \sigma_0 (1 + \rho_v) = \frac{9\pi^2 \nu^4}{N_0^2} \left(\frac{n_0^2 - 1}{n_0^2 + 2} \right)^2 \frac{3}{3 - 4\rho_v} (1 + \rho_v) . \quad (17)$$

In Eq. (17), N_0 is the number density for the reference condition at which n_0 (calculated from Bucholtz [23]) is determined. The gas component depolarization ratio ρ_v is calculated based on the dispersion relations from Bates [24]. At laser wavelength $\nu_L=308$ nm, the differential Rayleigh cross section is calculated to be $5.93 \cdot 10^{-27} \text{ cm}^2/\text{sr}$ and $5.86 \cdot 10^{-27} \text{ cm}^2/\text{sr}$ for our synthetic air and pure N_2 respectively. By varying the laser pulse energy, and/or the pressure of a buffer gas (N_2 or air) inside the calibration cell for the Hencken burner or in the same discharge cell for the plasma reactor, a linear plot of $S_{Rayleigh}$ vs. (NE) can be obtained, the slope ($D_{Rayleigh}$) of which is used to calculate the collection constant, $l\Omega\beta$, in Eq. (16). The final expression for absolute OH number density n_{OH} can be found by comparing Eq. (5) and Eq. (16) as follows:

$$n_{OH} = \frac{4\pi S_f \varepsilon_R \left(\frac{\partial \sigma}{\partial \Omega} \right)}{f_B b_{lu} E \phi_J D_{Rayleigh} hc \nu_L} . \quad (18)$$

6. Results and Discussion I: Temperature and OH Number Density in the Hencken Burner Flame

6.1 Laser Absorption and Fluorescence Trapping

OH absorbance was measured over both the $Q_1(9.5)$ transition (and the $P_{21}(9.5)$ satellite transition) and the $Q_2(6.5)$ transition (and the $R_{12}(6.5)$ satellite transition), and a sample trace with 13,200 data points is shown in Fig. 3. The sample location was across the center of the burner, 25 mm downstream from the surface. As can be seen, the baseline noise is very low, and thus the detection limit is very good (so good in fact that even the satellite transition could have been used for independent analysis). Of course in this flame, it is expected that OH concentration will be near an adiabatic, equilibrium value. The principal absorption

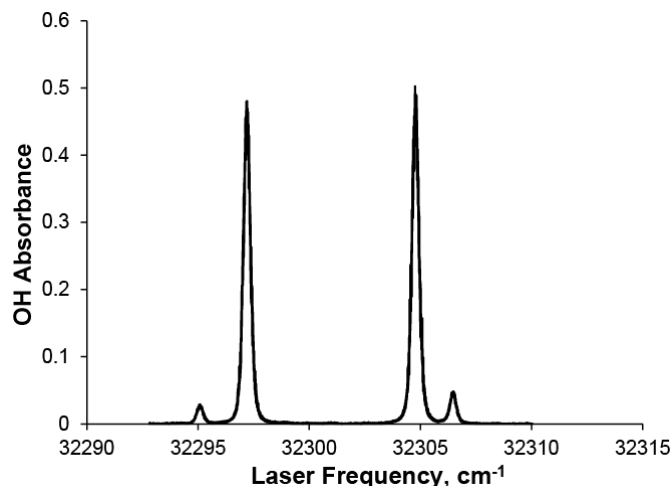


Figure 3: OH absorbance measured over both the $Q_1(9.5)$ transition (and its satellite, the $P_{21}(9.5)$ transition) and the $Q_2(6.5)$ transition (and its satellite, the $R_{12}(6.5)$ transition), in a near adiabatic CH_4 -air Hencken burner flame, at the burner center ($y=0$ mm) and 25 mm above the burner surface.

measurements were done in a single day, with six scans comparable to the one shown. Total integrated absorbance for both main branch transitions was calculated, and then using the derived path length (about 1.9 cm, for an LIF signal at $x=0$) and an assumed temperature of 2150 K, the number density was calculated using Eq. (2) and the iterative approach described above; it should be noted that both ground states are relatively insensitive to chosen temperature (especially the $J'=9.5$ state). For the twelve measurements, the derived number density varied by $< 2.5\%$ (total), and the average value was $0.918 (\pm 0.06) \times 10^{16} \text{ cm}^{-3}$, which is approximately equal to the equilibrium number density at 2170 K. It should be noted that this value was measured on a day with relatively high barometric pressure (751 torr), and the OH number density for days with lower barometric pressure were correspondingly smaller (about 1.5% with $P_{\text{bar}} = 741$ torr). A single absorption scan was also performed at 5 mm from the front edge of the burner ($y = -7$ mm), implementing the same process as described above. The OH number density obtained at this location was $0.72 \times 10^{16} \text{ cm}^{-3}$, which is approximately equal to the equilibrium number density at 2100 K.

Measurements to compare against the fluorescence trapping calculations were also performed. Here, the LIF was measured for different distances from the burner edge (closest to the camera), and OH absorption was measured at $y=0$ mm (burner center) and $y=-7$ mm. These measurements were then compared to the OH profile from an LIF line measurement, after rotating the burner by 90 degrees. The $P_{21}(9.5)$ satellite transition in the (0,0) band was chosen for fluorescence trapping study, as it experiences negligible laser attenuation. By translating the burner along its y -axis (refer to Fig. 1), the probing volume of the laser beam can be varied such that the consequential fluorescence signal experiences different trapping path lengths. In Fig. 4, the measured relative OH signal (red-square symbol) is plotted against laser probing location with regard to burner x -axis (refer to Fig. 1, the front edge is at $y=-12$ mm, the rear edge is at

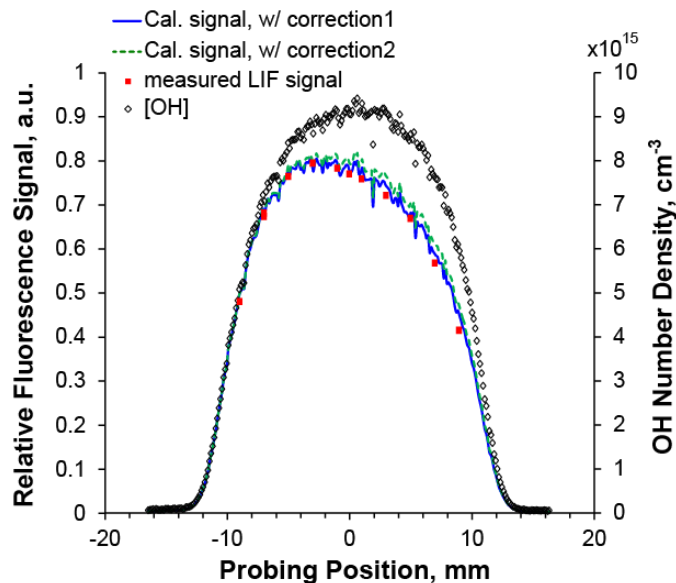


Figure 4: Fluorescence trapping along LIF signal travel path in a near adiabatic CH₄-air Hencken burner flame, at the burner center ($y=0$ mm) and 25 mm above the burner surface. The laser probing location is measured by its distance from the burner x-axis (Figure 1) along the burner y-axis. The front and rear edges are corresponding to probing position $y=-12$ mm and 12 mm respectively. The calculated signal is based on the measured OH profile along the burner y-axis.

$y=12$ mm). The detailed OH profile was across the same axis as the trapping (y -axis) measurement, obtained using the ICCD camera after the burner was rotated. It is plotted in Fig. 4 (hollow-diamond symbol) on the secondary vertical axis as a reference. Relative fluorescence signal is also calculated by correcting the measured OH profile with corresponding trapping ratios following the discussion in Section 4.4. Two different trapping corrections are applied separately: *i) correction 1* is based on the non-thermal assumption, i.e., Eq. (14); *ii) correction 2* is based on thermal assumption, i.e., Eq. (15). The temperature used for trapping calculation is assumed to be $T=2150$ K, same as in the absorption measurements discussed above. Measured LIF signal is rescaled to match with the OH profile at 5 mm inward of the near edge (i.e., at $y=-7$ mm). As can be seen, for this particular transition, both correction methods match well with the measured trapping, with *correction 2* predicting slightly less trapping than *correction 1*. For directly excited J' levels that reside away from the peak of thermal population distribution in $v'=0$ ($J'=6.5$ at 2150 K), one can expect a larger difference between thermal and non-thermal corrections for trapping. .

6.2 OH LIF Signal Correction and Thermometry

OH LIF was measured 25 mm above the Hencken burner surface by both (0,0) and (1,0) excitation schemes. All the experimental results shown in the figures here were taken at the center of the burner ($y=0$ mm) by exciting R-branch transitions in the OH A-X (0,0) band system. Fig. 5 plots the laser transmittance at the transition center ($v=v_0$) along the laser beam

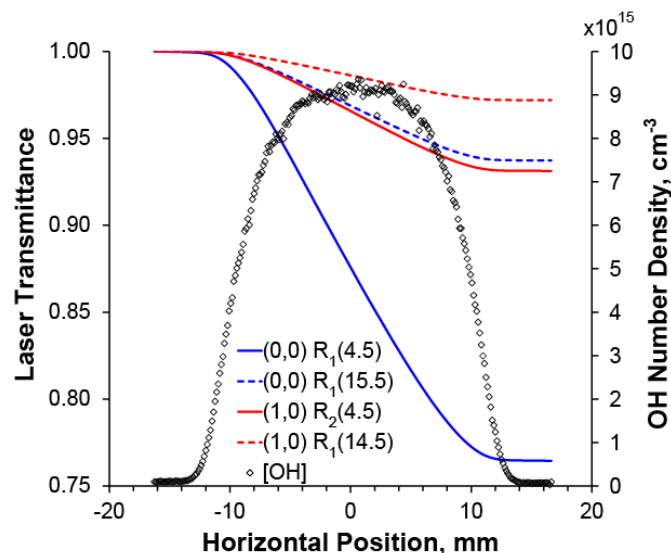


Figure 5: Laser beam attenuation in a near adiabatic CH_4 -air Hencken burner flame, at the burner center ($y=0$ mm) and 25 mm above the burner surface. The horizontal position corresponds to the burner x-axis (Figure 1). The laser beam travels in the positive direction of the x-axis.

propagation direction (x-axis of the burner, refer to Fig. 1), calculated by comparing the modified overlap integral g' (Eq. (12)) with the original g (Eq. (4)), based on the measured OH concentration profile and at $T=2150$ K. The laser linewidth used to calculate the transmittance is 0.75 cm^{-1} , estimated for the LIF system at OSU, but the results are only a weak function of laser linewidth. From Fig. 5, the transmittance difference between $R_1(4.5)$ and $R_1(15.5)$ in the (0,0) band is about 9% averaged across the sampling volume (approximately from $x=-1.5$ mm to 1.5 mm) when the laser is tuned to the peak of the transition. If not corrected for, this would cause about 3% rise in best fit temperature (about 60 K) in the experimental flame condition. For (1,0)

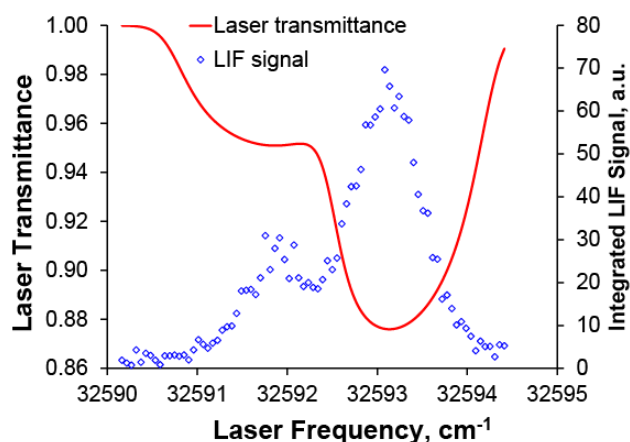


Figure 6: A sample laser absorption correction applied to an experimental LIF spectrum taken by scanning the laser across $R_1(4.5)$ and $Q_{21}(4.5)$ transitions in the OH A-X (0,0) band, in a near adiabatic CH_4 -air Hencken burner flame, at the burner center ($y=0$ mm) and 25 mm above the burner surface.

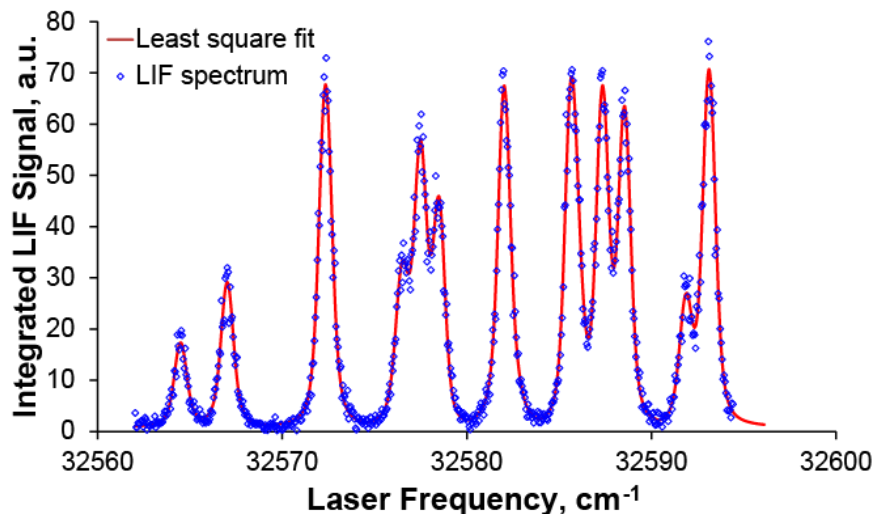


Figure 7: A sample LIF excitation spectrum fitted with Voigt profile. The LIF spectrum is taken by scanning the laser across 14 major transitions in the R-branch in the OH A-X (0,0) band in a near adiabatic CH₄-air Hencken burner flame, at the burner center ($y=0$ mm) and 25 mm above the burner surface. It is corrected by laser attenuation during the fitting process.

excitation, laser absorption seems to have negligible effect on temperature inference. By choosing relatively weak excitation transitions (especially in the (1,0) band), one can avoid significant signal correction caused by laser absorption, the uncertainty of which may be carried into temperature inference.

Since an excitation scan was performed in the present work, the laser attenuation correction varies with laser wavelength, as described by Eq. (13). This is shown in Fig. 6, which plots an experimental excitation spectrum (hollow diamond) consists of R₁(4.5) and Q₂₁(4.5). The dye laser was scanned with 0.0005-nm (at the UV wavelength) steps at 10 shots per step. The median of the 10 shots was taken to represent the signal at that wavelength. This spectrum

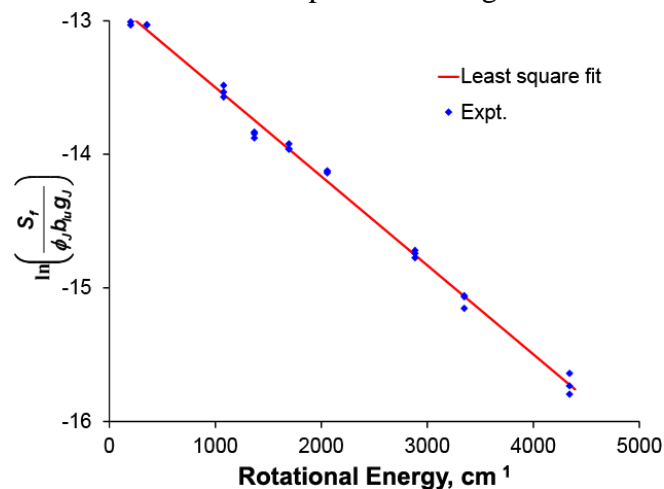


Figure 8: Temperature inference with Boltzmann fit of integrated LIF spectra from transitions shown in Fig. 7. Only 9 of the 14 transitions are distinguishable from the fit and are integrated separately. The best fit temperature is 2160 ± 61 K with $R^2=0.9952$.

shown here was only corrected by monitored laser energy (measured before the flame). The laser transmittance, i.e., g/g (averaged over 3-mm-long sampling volume) is plotted in the red solid line. The original spectrum is then divided by the transmittance before it is fitted and integrated, as explained in Section 4.3.

Figure 7 shows an experimental excitation spectrum collected by continuously tuning the dye laser across 14 transitions in the R-branch of OH A-X (0,0) band, many of which are blended into each other due to the broad laser source. A sample of the least-squares Voigt fit is plotted alongside the experimental spectrum. The benefit of the fit, as mentioned in Section 4, is that it enables us to distinguish each transition from the fitting results and integrate them separately. Notice that, $R_2(10.5)$ and $R_1(14.5)$ (at about 32585 cm^{-1}) are too close to each other ($\Delta v = 0.3 \text{ cm}^{-1}$) to be resolved by the laser source. As a result, the fitting results for these two transitions are not reliable, and these transitions are excluded from the fit. Satellite transitions are discarded for the same reason. The remaining 9 transitions (from $J'' = 3.5$ to 15.5) obtained from the Voigt fit in Fig. 7 are integrated and corrected for fluorescence trapping and quantum yield, then fitted to the Boltzmann relation (Eq. (7)) to infer the OH rotational temperature, as shown in Fig. 8. Here Correction 1 (non-thermal assumption) is used to estimate the trapping ratio and the radiative decay rate of transitions originated from $v'=0$. The best fit temperature is $2160 \pm 61 \text{ K}$, with $R^2 = 0.9952$. Temperatures inferred from OH LIF thermometry with both (0,0) and (1,0) excitation are summarized in Table 1.

Table 1: Summary of LIF thermometry

Excitation	Range of J''	Location	Correction	T (K)	Error \pm (K)
(0, 0)	2.5-15.5	$y = -7 \text{ mm}$	1	2059	77
			2	1922	64
	3.5-15.5	$y = 0 \text{ mm}$	1	2160	61
			2	2113	43
(1, 0)	2.5-14.5	$y = -7 \text{ mm}$	3	1983	70
			4	1892	62
		$y = 0 \text{ mm}$	3	2223	51
			4	2118	42

For (1,0) excitation, Correction 3 is based on the assumption that emission from $v'=1$ is non-thermal but thermal for $v'=0$; Correction 4 is assuming thermalized condition for both $v'=1$ and $v'=0$. Note that for thermalized corrections (2 and 4), the same trapping transmittances and radiative decay rate are applied to different transitions (no transition dependence). The non-thermal correction has the effect of raising inferred temperature, because low- J' transitions have larger radiative decay rates than do high- J' transitions. The trapping correction on the other hand, has an opposite effect. For (0,0) excitation, the calculated trapping transmittance is greater than 80% at the center (at $y=0 \text{ mm}$), and greater than 95% at near the edge (at $y=-7 \text{ mm}$). The relative

difference between low- and high- J' transitions in trapping transmittance is less than 15%, slightly lower than the difference found in the total radiative decay rate; therefore, the overall effect of the non-thermal correction is a higher temperature than with the thermalized correction (see Table 1). Similar comparison can be made for temperatures inferred from (1,0) excitation scheme. However, due to population redistribution by VET, the simple thermal and non-thermal assumptions may introduce systematic error in the calculation of total radiative decay rate (trapping is quite small and varies little among different transitions), and hence in the inferred temperature. In the current work, for the best agreement with absorption measurements, temperatures measured by (0,0) excitation with the non-thermal correction are used for calculating Boltzmann factors. Nonetheless, the differences between temperatures inferred by the two corrections methods are not large.

6.3 Calibration with Rayleigh Scattering

For the Rayleigh scattering measurement, the laser wavelength was tuned to 308 nm and the small calibration quartz cell was mounted above the burner surface such that the laser beam passed through its center. No alignment change was involved in signal collection. The incoming laser beam was vertically polarized, as with the LIF measurements. The effect on laser beam energy and signal collection efficiency due to the inclusion of the calibration cell was experimentally determined to be negligibly small. Laser scattering background was determined by recording PMT signal at various laser energies when the calibration cell was evacuated ($P < 1$ torr). By varying the gas pressure and laser energy, a linear relation between Rayleigh signal and the product of gas number density (N) and laser energy (E) can be derived. Figure 9 shows one

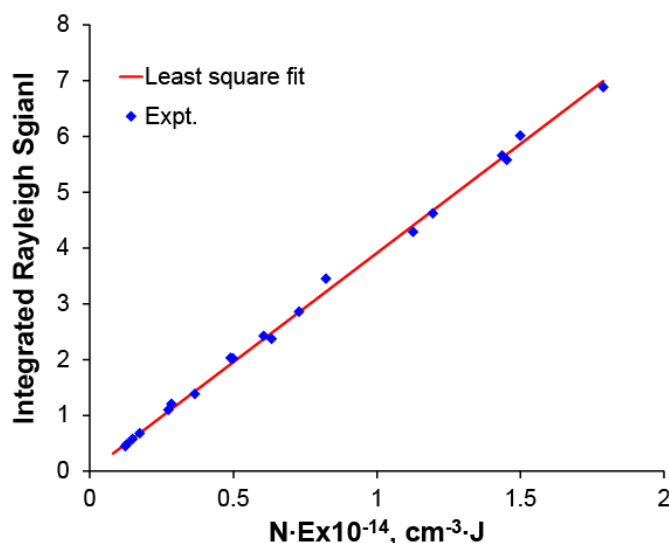


Figure 9: A sample linear fit of Rayleigh scattering signal measured in pure N_2 in the calibration vacuum cell placed above the burner vs. the product of N_2 number density and laser energy. The slope of the linear fit contains the optical collection constant necessary for calibrating absolute OH concentration

set of Rayleigh scattering data in pure N_2 at room temperature. The slope of the linear fit is used to calculate collection constant $l\Omega\beta$. Multiple runs in both air and pure N_2 at room temperature were conducted and the average calculated collection constant was used to calibrate the relative OH concentration measured by both (0,0) and (1,0) transitions. The results are summarized in Table 2 and compared with OH number densities obtained from laser absorption measurements. The least temperature sensitive transition (in the range of 2000-2500 K) among all the transitions used in temperature measurement is used to derive number density. The standard deviation of the absolute number density values among all transitions is about $\pm 5\%$. Note that for signals taken at $y=-7$ mm, laser attenuation and modified overlap integral are calculated based on an OH profile at $y=-7$ mm across the burner x-axis, taken with the same method used at $y=0$ mm. The uncertainty in the OH number density from OH LIF, by taking into account standard deviation of run-to-run, statistical uncertainty in fittings, uncertainty in measured temperature, and other uncertainties from absorption coefficient, Rayleigh cross section, and measured laser energy, is estimated to be $\pm 15\text{-}20\%$, with laser energy measurement and standard deviation in the calibration constants measured by Rayleigh scattering being the major sources of uncertainty. For the absorption measurements, the uncertainty in OH concentration is estimated to be better than $\pm 10\%$.

Table 2: Summary of Measured Absolute OH Number Density

Excitation	Transition	Location	Correction	N_{OH} (10^{15} cm^{-3})	$N_{OH, \text{absorp}}$ (10^{15} cm^{-3})
(0,0)	$R_2(12.5)$	$y=-7$ mm	1	7.11	7.20
			2	6.43	
	$R_2(9.5)$	$y=0$ mm	1	8.64	9.20
			2	8.40	
(1,0)	$R_1(11.5)$	$y=-7$ mm	3	7.27	7.20
			4	7.42	
	$R_1(11.5)$	$y=0$ mm	3	8.93	9.20
			4	8.64	

As can be seen in Table 2, by choosing temperature insensitive transitions (near the peak of thermal population distribution in $v''=0$), thermal and non-thermal correction methods yield very similar results. As noted during the discussion of trapping correction, if the excited J' level is far from the peak of the thermal population distribution in $v'=0$ or $v'=1$, the difference in trapping correction can be noticeable (e.g., about 10% higher trapping with thermal correction for $R_1(15.5)$ in the (0,0) band)). Nevertheless, by taking into account the overall uncertainty ($\sim 20\text{-}30\%$), absolute OH number densities calibrated by Rayleigh scattering agree reasonably well with laser absorption measurements, for all the cases obtained with both (0,0) and (1,0) excitation schemes and corrected by either non-thermal or thermal assumptions for trapping and

total radiative decay rate. It is therefore concluded that Rayleigh scattering can be a valid calibration approach for absolute OH concentration measurement.

7. Results and Discussion II: Absolute OH Concentration Measurements in the Low Pressure Plasma Reactor

7.1 Spatial Uniformity of the Plasma

Plasma uniformity is difficult to quantify but critical for isolating nonequilibrium chemistry effects from thermal heating occurring in filaments and hot spots. The approach used for sustaining diffuse, nearly zero-dimensional nsec pulse discharges in plane-to-plane geometry was discussed in detail in our previous work [9, 25]. Before quantitative OH LIF measurements are performed, plasma uniformity is verified qualitatively by taking images employing an ICCD camera during individual discharge pulses. Time-resolved, broadband, single-shot images taken during a high voltage nsec pulse discharge in air at $T_0=500$ K and $P=50$ torr, using a PI-MAX ICCD camera and a UV lens (Sodern 100-mm f/2.8), are shown in Fig. 10. The camera gate is set at 490 psec and synchronized with the high voltage pulse generator to open during the last pulse in a 10-pulse discharge burst, with $t=0$ representing the beginning of the pulse. The timing of the gate is indicated on the top of each image. The images capture primarily nitrogen second positive band emission, $N_2 C^3\Pi \rightarrow B^3\Pi$. To isolate plasma emission from the reflections from the

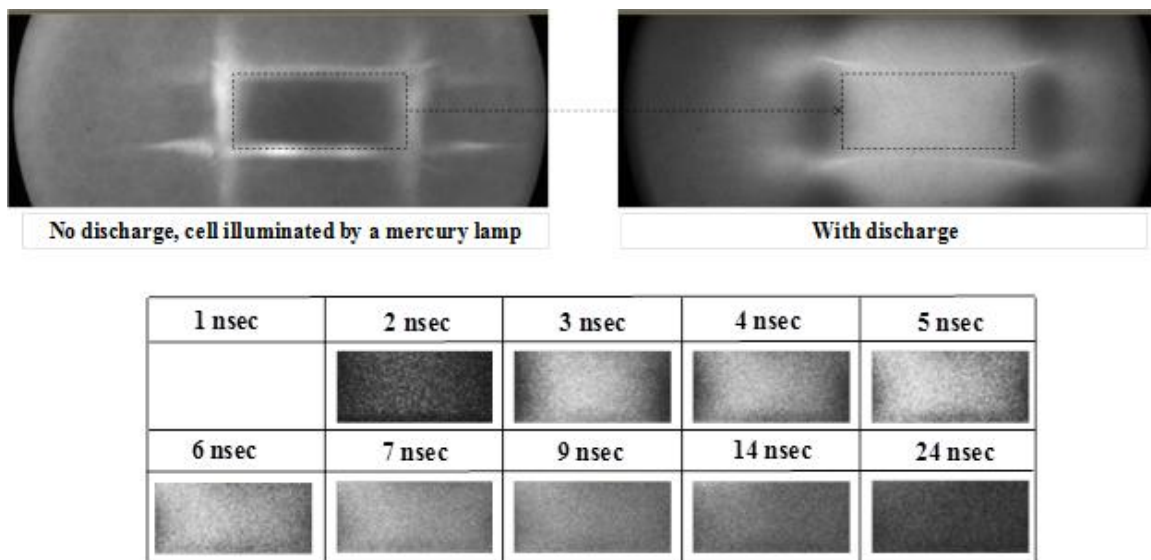


Figure 10: Top: ICCD images of the flow channel without the discharge and with the discharge, taken through the window at the end of the channel. Extracted region corresponds to the channel cross section (22 mm x 10 mm). Bottom: images of the plasma during a single discharge pulse (pulse #10 in the burst) in air at the conditions of Fig. 2, taken through the same window and showing the entire channel cross section. Camera gate 490 psec, timing of the gate is shown on top of each image.










	Pulse #1	Pulse #10	Pulse #100
Air, $T_0=500$ K, $P=200$ torr			
H_2 – air, $\phi=0.3$ $T_0=500$ K, $P=100$ torr			
C_2H_4 – air, $\phi=0.3$ $T_0=500$ K, $P=100$ torr			

Figure 11: ICCD images of the plasma in and fuel-air mixtures preheated to $T_0=500$ K, taken through the window in the end of the channel. $\nu=10$ kHz, camera gate = 50 nsec, images show the entire channel cross section (22 mm x 10 mm).

channel walls, images were taken with and without the discharge, and a rectangular region corresponding to the channel cross section (22 mm x 10 mm) was extracted from the original images. From the images in Fig. 10, it is evident that the plasma was generated in the entire volume between the electrodes and remains diffuse and nearly uniform until it decayed completely. Total emission intensity (a sum of intensity counts over all pixels in each ICCD image) decays very rapidly after each discharge pulse, on the time scale of a few nsecs, demonstrating that excited radiating species (mainly N_2 $C^3\Pi$ state) are quenched rapidly. Previous plasma images taken from the side of the test cell via the right angle prism demonstrates similar uniform, volume-filling discharge.

As discussed in our previous work [9], increasing pressure and / or adding H_2 or hydrocarbons to the air plasma makes the discharge less uniform and results in formation of well-defined filaments, due to development of ionization – heating instability. This effect is especially well pronounced in hydrocarbon-air mixtures at pressures of ~ 100 torr and above, although mild preheating to $T_0=400$ -500 K reduces the nonuniformity considerably. Fig. 11 shows ICCD images (50-nsec exposure) of discharges in air, H_2 -air ($\phi=0.3$), and C_2H_4 -air ($\phi=0.3$) preheated to $T_0=500$ K, taken through the window in the end of the channel. These images illustrate that the plasma remains diffuse and filament-free at these conditions. As in Fig. 10, the images show the entire channel cross section (22 mm x 10 mm). Note, however, that nsec pulse plasma-assisted ignition in CH_4 -air and C_2H_4 -air mixtures still exhibits a well-defined propagating flame [9], such that near-homogeneous ignition could not be achieved. In the present work, this problem is circumvented by employing short discharge bursts (50 pulses at the pulse repetition rate of $\nu=10$ kHz, far less than needed for ignition) and operating in fuel-lean mixtures below the flammability limit, with the main emphasis of measuring OH number density in the plasma prior to ignition. As discussed in Section 2, LIF signal from (0,0) excitation is collected from the region in the center of the plasma approximately 3 mm long, where the plasma is uniform in both side view and front view (taken through the end window) ICCD images. This

eliminates the effect of discharge nonuniformity that may be found near electrode edges at high pressures [9].

7.2 OH Number Density after the Discharge

Temperature in the experimental conditions in the plasma reactor used in the current work has been measured previously with both OH LIF thermometry and CARS measurements [7], demonstrating good agreement between the two methods. Temperatures at the end of the discharge burst, measured by these two techniques, are in the range of $T=550-580$ K, indicating a modest temperature rise of 50-80 K occurs in the discharge burst, consistent also with kinetic modeling predictions. The temperature after the burst remains essentially unchanged, for up to a 10 msec delay. N_2 vibrational temperatures inferred from CARS measurements are quite low, $T_v \approx 850$ K in air and $T_v \approx 600-700$ K in fuel-air after a 50-pulse burst, demonstrating that vibrational nonequilibrium is not a significant factor at the present conditions [7]. An average temperature $T=570$ K is used when calculating Boltzmann factor for LIF signal reduction.

As discussed in Section 4, total decay time $1/(A_0+Q_0)$ can be determined from fitting the fluorescence decay with a single exponential fit. Figure 12 shows a sample time-resolved LIF pulse signal (50-shot averaging) taken in H_2 -air ($\phi=0.03$) with $R_1(4.5)$ in the (0,0) band. The fluorescence decay about 20 nsec after the initial signal rise is fitted to a single exponential function, with a best fit of $\tau=12.79 \pm 0.1$ nsec ($R^2=0.9969$). The quenching rate inferred from the total decay time is $7.68 \cdot 10^7 \text{ sec}^{-1}$ (with A coefficient calculated by thermal assumption for $v'=0$). The total decay rate remains nearly constant over 1 msec after the discharge burst, as shown in Fig. 13. Fluorescence decay time inferred from (1,0) excitation at the same condition in our previous work [7] is also plotted here. As the case shown in Fig. 13, it is found that the total decay time measured by (1,0) excitation is systematically lower than that from (0,0) excitation in

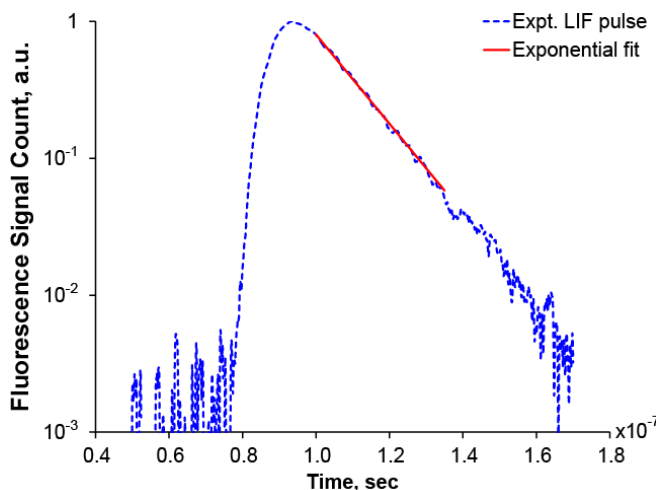


Figure 12: A sample time-resolved fluorescence signal pulse measured by exciting $R_1(4.5)$ in the OH A-X (0,0) band in a $\phi=0.03$ H_2 -air mixture at $T_0=500$ K and $P=100$ torr, 3 μsec after the gas mixture is excited by a 10 kHz, 50 pulses nanosecond pulse discharge burst. The fluorescence total decay time inferred from the exponential fit is $\tau=1/(A_0+Q_0)=12.79 \pm 0.1$ nsec ($R^2=0.9969$).

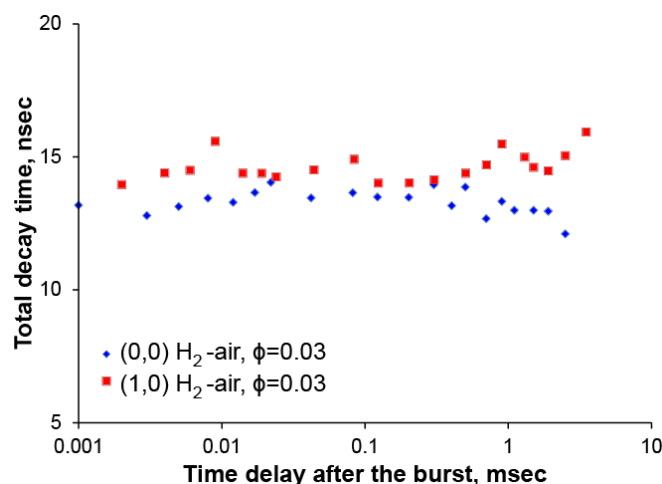


Figure 13: Measured total decay time in a $\phi=0.03$ H₂-air mixture at $T_0=500$ K and $P=100$ torr, with time delay after the gas mixture is excited by a 10 kHz, 50-pulse discharge burst. The total decay time is determined by fitting fluorescence decay, taken with both $Q_1(3.5)$ in (1,0) (from [7]) and $R_1(4.5)$ in (0,0) excitation schemes.

all fuel-air mixtures studied in this work. After obtaining the quantum yield, OH signal taken from (0,0) excitation is put on an absolute scale by calibrating against Rayleigh scattering signal, measured in the same plasma reactor at room temperature, using the approach described in Section 6.3. For each fuel, OH concentration at two equivalence ratios (the second and fourth richest cases shown in Figs. 15-17) is measured using the (0,0) excitation scheme and calibrated by Rayleigh scattering. The absolute concentration calibration constant for OH LIF recorded with (1,0) excitation (from ref. [7]) can then be determined, and all of the data points are plotted in Figs. 15-17. The absolute number density inferred from the plasma reactor has an estimated uncertainty of about $\pm 20\%$.

To obtain insight into kinetics of plasma/chemical fuel oxidation and ignition, we use a kinetic model developed in our previous work [4, 6, 8, 26]. Briefly, the model incorporates nonequilibrium air plasma chemistry [27], expanded to include hydrocarbons and hydrogen dissociation processes in the plasma [26, 28]. In the present work, the plasma chemical reaction set is also expanded to incorporate C₃H₈ dissociation reactions by electronically excited N₂ [29]. The plasma chemistry model is coupled with one of two “conventional” hydrogen-oxygen chemistry mechanisms developed by Popov [28] and Konnov [30], and one of the three hydrocarbon chemistry mechanism: a) GRI Mech 3.0 [31]; b) USC / Wang mechanism [32]; or c) Konnov mechanism [33]. Note that the mechanisms have been developed and validated for relatively high-temperatures, significantly higher than found in the present experiments, and may well be inaccurate at the present conditions. Assessing applicability of these mechanisms, used as a starting point for development of a nonequilibrium plasma assisted combustion mechanism, is one of the objectives of the present work.

Figure 14 plots absolute, time-resolved [OH] measured in lean H₂-air mixtures at $T_0=500$ K and $P=100$ torr vs. time delay after a $\nu=10$ kHz, 50-pulse discharge burst, at different

equivalence ratios ($\phi=0.015$ - 0.12). Rotational temperatures measured by LIF thermometry at the end of the burst (time delay 2 μsec after the burst) at these conditions are also shown in Fig. 14(circled). It can be seen that peak $[\text{OH}]$ after the burst, $(3.0$ - $3.6)\cdot 10^{13} \text{ cm}^{-3}$, is not sensitive to the equivalence ratio in this range. Also, there is essentially no transient $[\text{OH}]$ rise after the burst. The fairly long $[\text{OH}]$ decay time, ~ 0.5 - 1.0 msec, shows that it accumulates during the 10 kHz burst (time interval between the pulses of 0.1 msec), consistent with our previous results in H_2 -air at a discharge pulse repetition rate of $\nu=40$ kHz [8]. Temperature measured at the end of the discharge burst by OH LIF thermometry with (1,0) excitation from our previous work [7] (also plotted here) is not very sensitive to the equivalence ratio and delay time after the discharge [7] and remains within the range of $T=540$ - 580 K (see Fig. 14).

Figure 14 also compares kinetic model predictions with the experimental results, using two different “conventional” H_2 -air chemistry mechanisms developed by Popov [28] (Fig. 14 (a))

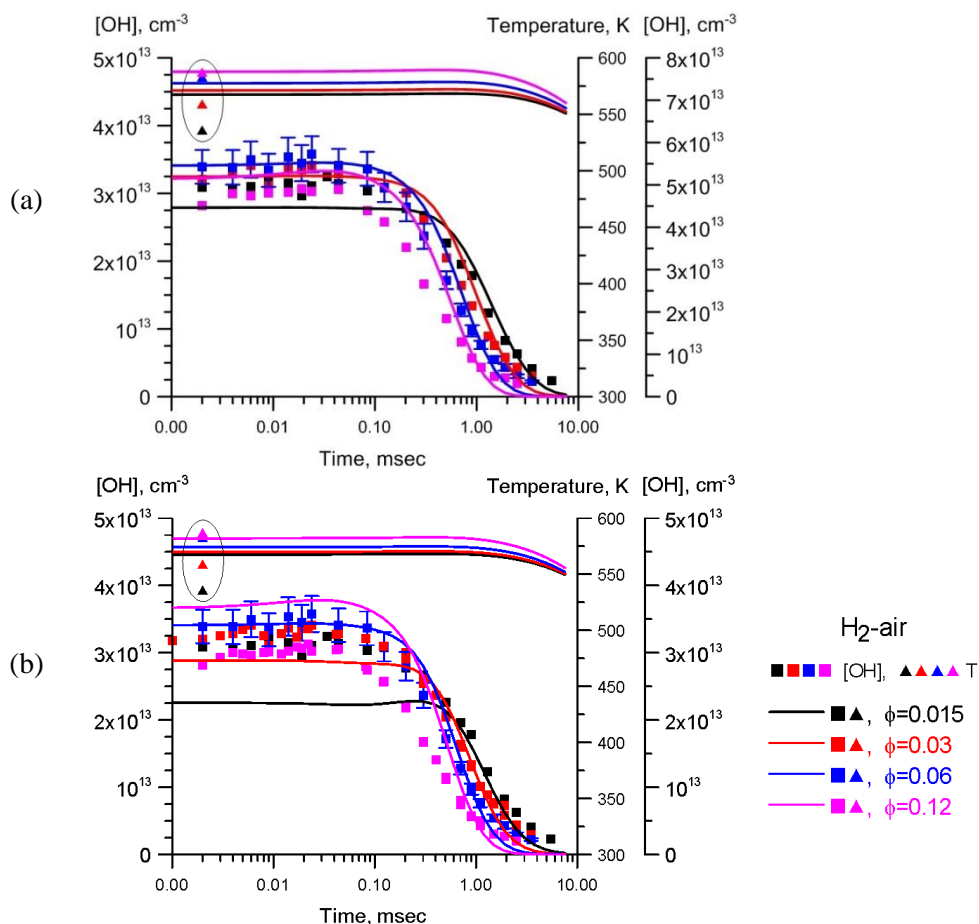


Figure 14: Comparison of experimental (y-axis on the left) and predicted (y-axis on the right) time-resolved, absolute OH number densities after a $\nu=10$ kHz, 50-pulse discharge burst in H_2 -air mixtures at $T_0=500$ K, $P=100$ torr, and different equivalence ratios. Data points for temperatures measured at the end of the burst (time delay 2 μsec) are circled.

- (a) Popov mechanism
- (b) Konnov mechanism

and Konnov [30] (Fig. 14 (b)). Note that the model predictions for [OH] are plotted using the vertical axis on the right-hand side of the figures, while the experimental data are shown using the vertical axis on the left-hand side. As can be seen, the Popov mechanism matches the weak dependence of [OH] on the equivalence ratio (by 50-60%) but consistently overpredicts absolute [OH] and somewhat overpredicts the [OH] decay time at the higher equivalence ratio of $\phi=0.12$ (see Fig. 14 (a)). On the other hand, the Konnov mechanism matches absolute [OH] concentration as well as decay time (except at $\phi=0.12$) but shows a somewhat greater dependence of peak [OH] on the equivalence ratio than seen in the experimental results. Kinetic sensitivity analysis has shown that the difference between the two mechanisms is almost entirely due to the difference in the rate coefficients of reaction $O + OH \rightarrow H + O_2$, $k=1.2 \cdot 10^{-11} \text{ cm}^3/\text{s}$ [28] and $k=5.3 \cdot 10^{-11} \text{ cm}^3/\text{s}$ [30] at $T=500 \text{ K}$ (while the value suggested in a recent review [34] is $k=3.0 \cdot 10^{-11} \text{ cm}^3/\text{s}$).

The results in lean CH_4 -air mixtures are shown in Fig. 15. Unlike in H_2 -air mixtures, peak [OH] after the burst is reduced as the equivalence ratio increased, by about 50% between $\phi=0.03$ and $\phi=0.24$. Like found with H_2 -air mixtures, almost no transient [OH] increase is observed, except for a modest rise at $\phi=0.24$. The [OH] decay time in CH_4 -air is somewhat shorter than in H_2 -air, ranging from $\sim 1 \text{ msec}$ at $\phi=0.03$ to $\sim 0.2 \text{ msec}$ at $\phi=0.24$. Again, this suggests fairly significant OH accumulation during the discharge burst at the pulse repetition rate of $\nu=10 \text{ kHz}$. At the higher equivalence ratio, $\phi=0.24$, a modest transient [OH] overshoot after the burst is apparent. [OH] after the discharge burst predicted by two “conventional” hydrocarbon-air chemistry mechanisms, GRI 3.0 [31] and USC / Wang [32], are relatively close to each other (see Fig. 15 (a,b)), both exceeding peak measured [OH] by 60-100%. Both mechanisms reproduce weak transient [OH] rise in higher equivalence ratio mixtures, with Wang mechanism showing better agreement with [OH] decay after the burst. The Konnov mechanism, on the other hand, matches absolute [OH], the weak transient rise, and the [OH] decay relatively well (see Fig. 15 (c)). Comparison with the modeling calculations shows clearly that both peak [OH] and decay time reduction at higher equivalence ratios are primarily due to increase in net rate of radical removal via fuel oxidation reactions, since coupled discharge pulse energy and the net rate of radical generation are nearly independent of the equivalence ratio.

Figure 16 plots the results in lean C_2H_4 -air mixtures. It can be seen that in the entire range of equivalence ratios, [OH] after the burst first increases, by up to 60%, before eventually decaying. Similar to the results in CH_4 -air mixtures, increasing the equivalence ratio reduces peak transient [OH] after the burst by approximately a factor of 2, from $\approx 2 \cdot 10^{13} \text{ cm}^{-3}$ at $\phi=0.05$ to $\approx 1 \cdot 10^{13} \text{ cm}^{-3}$ at $\phi=0.36$ (see Fig. 16). Finally, [OH] decay time is much shorter than in H_2 -air and CH_4 -air and is reduced considerably as the equivalence ratio is increased, from $\sim 0.1 \text{ msec}$ at $\phi=0.05$ to $\sim 0.03 \text{ msec}$ at $\phi=0.36$. This shows that no significant OH accumulation occurs during the discharge burst, since [OH] decay time is comparable with time delay between the pulses in a 10 kHz burst. Again, these trends (both peak [OH] and decay time reduction) are due to more rapid net rate of radical removal via fuel oxidation reactions at the higher equivalence ratio. As can be seen, GRI 3.0 mechanism overpredicts both peak [OH] and decay time, by a factor of 3-4.

The USC / Wang mechanism performs noticeably better, although peak [OH] and decay time are still underpredicted by about a factor of 2 (except at higher equivalence ratio, $\phi=0.36$, where the model underpredicts the decay time by about a factor of 4). Finally, the Konnov mechanism reproduces both peak [OH] and its decay in very lean mixtures well, although the agreement is not as good as the equivalence ratio is increased.

Based on the comparison of the present experimental results with kinetic modeling, the Konnov mechanisms for H_2 -air, CH_4 -air, and C_2H_4 -air show better overall agreement with our measurements, compared to the Popov, GRI 3.0, and USC / Wang mechanisms. Note that kinetic modeling shows that significant transient [OH] rise after the burst, observed in C_2H_4 -air, is not due to chain branching processes, which remain insignificant at these low temperatures. In fact, it is produced primarily by O and H atoms generated by electron impact and by quenching of electronically excited nitrogen during and immediately after the last pulse in the burst (within $\sim 1 \mu\text{sec}$ [10]).

The experimental results in C_3H_8 -air are very similar to those in C_2H_4 -air (compare Fig. 16 and Fig. 17). In both fuel-air mixtures, peak [OH] is reduced as the equivalence ratio is increased, exhibiting a transient rise after the burst, and the [OH] decay rates in these two fuel-air mixtures are similar. However, kinetic modeling significantly overpredicts peak [OH] (by a factor of 3 for GRI 3.0, a factor of 6 for USC / Wang, and a factor of 2 for Konnov). Also, [OH] decay time is overpredicted considerably by all three mechanisms, and the significant transient rise in the lean mixture ($\phi=0.04$) is not reproduced by any of them. In particular, predictions from the Konnov mechanism, which performs relatively well in H_2 -air, CH_4 -air, and C_2H_4 -air, are at variance with the experimental results in C_3H_8 -air.

We believe that these differences are primarily due to uncertainties in “conventional” C_3 chemical reaction pathways and rates. Indeed, the fuel fraction in the leanest C_3H_8 -air mixture tested ($\phi=0.04$) is only 0.18%, suggesting that dominant plasma chemical radical generation processes occur during electron impact excitation and quenching of excited N_2 and O_2 , within $\sim 1 \mu\text{sec}$ after the burst. Kinetics of these processes appear to be captured by the present plasma chemical model (using Konnov mechanism) relatively well, since the model predictions in very lean H_2 -air, CH_4 -air, and C_2H_4 -air are close to the experiment values. Thus, the present data show the need for development of an accurate, predictive plasma chemistry / fuel chemistry kinetic model that would be applicable to fuels C_3 and higher. Also, tracing the cause of the differences between different fuel-air kinetic mechanisms to individual species and reactions requires detailed sensitivity analysis, which will be undertaken in our future work.

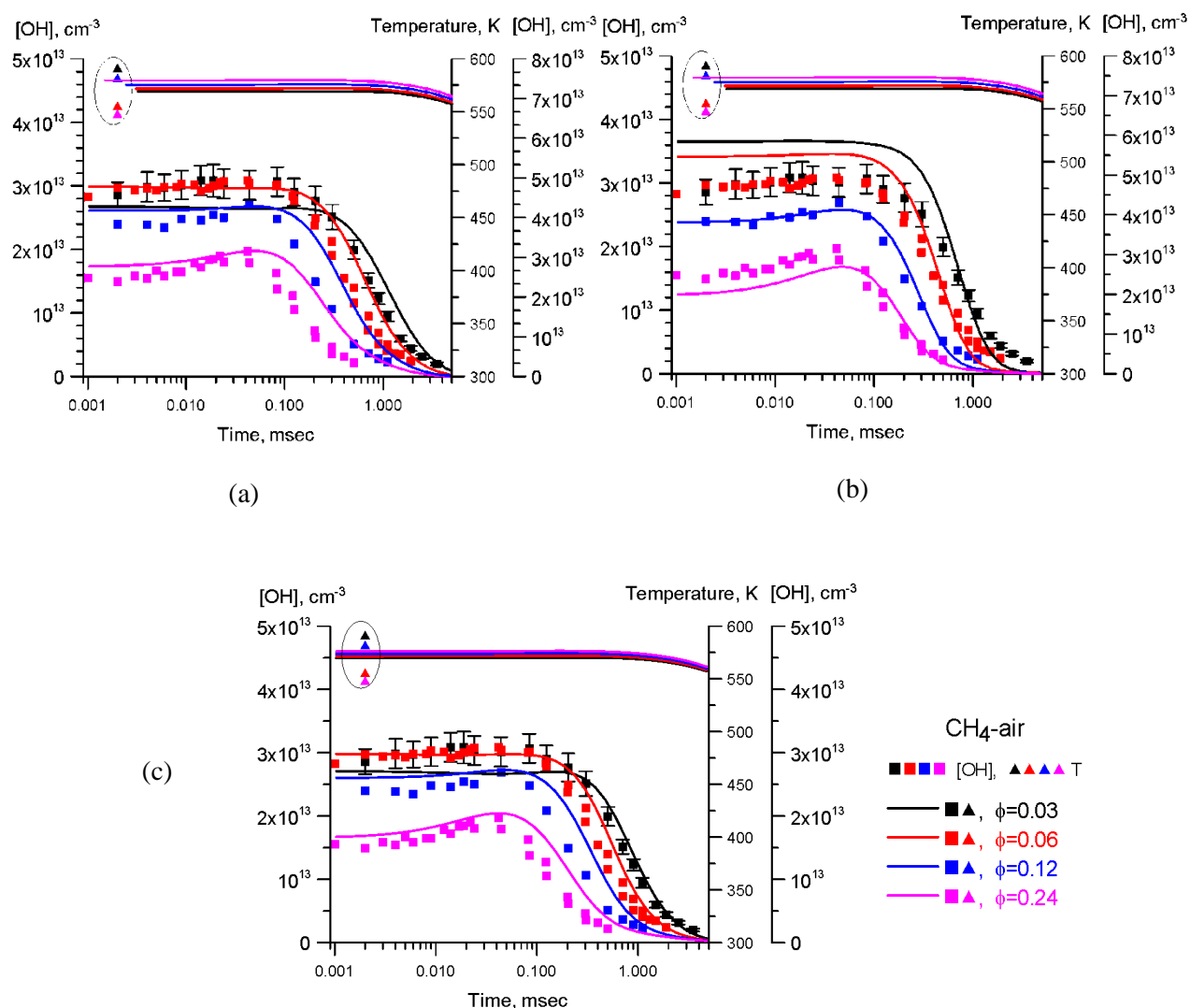


Figure 15: Comparison of experimental (y-axis on the left) and predicted (y-axis on the right) time-resolved, absolute OH number densities after a $\nu=10$ kHz, 50-pulse discharge burst in CH_4 -air mixtures at $T_0=500$ K, $P=100$ torr, and different equivalence ratios. Data points for temperatures measured at the end of the burst (time delay $2 \mu\text{sec}$) are circled.

- (a) GRI 3.0 mechanism
- (b) USC / Wang mechanism
- (c) Konnov mechanism

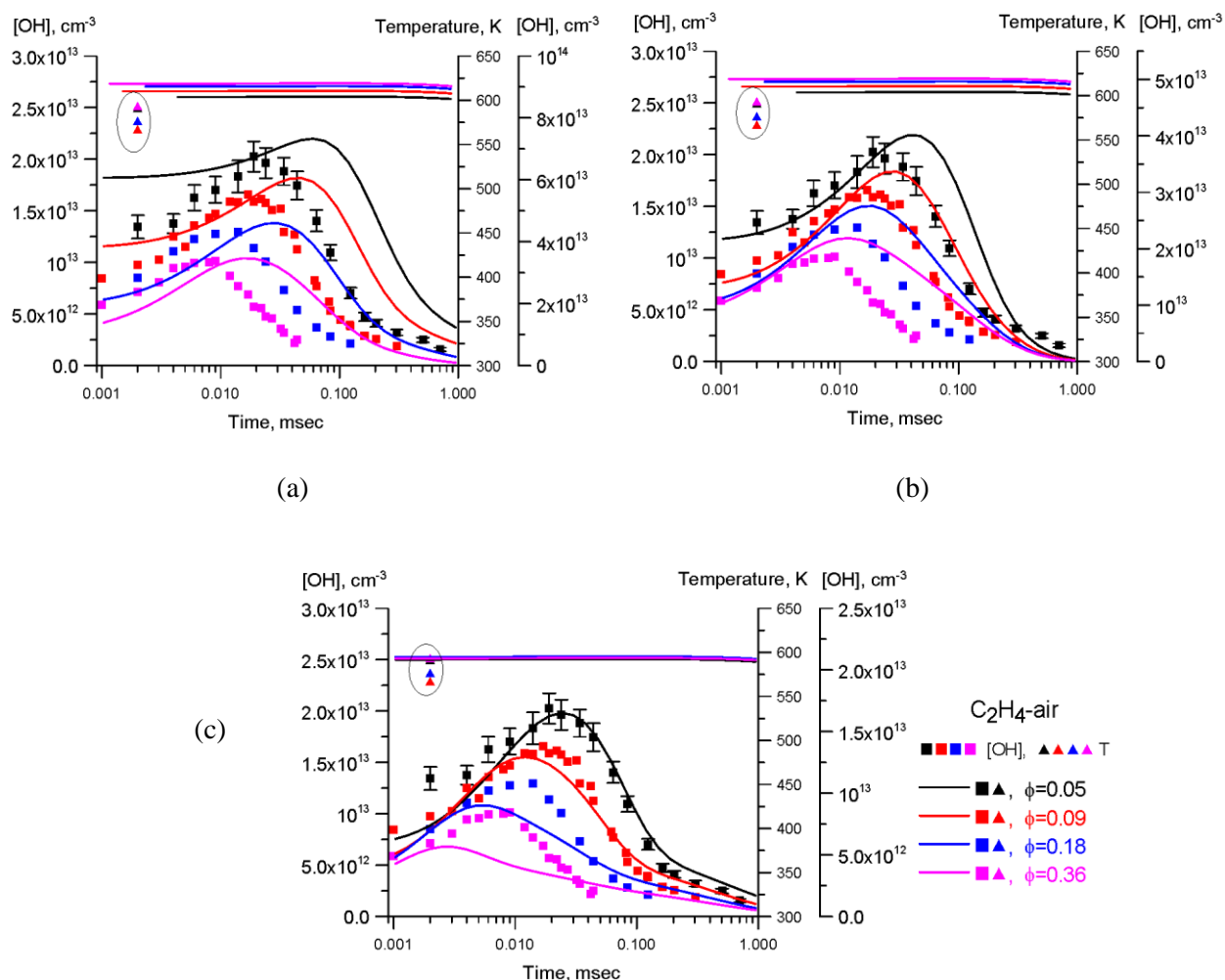


Figure 16: Comparison of experimental and predicted time-resolved, absolute OH number densities after a $\nu=10$ kHz, 50-pulse discharge burst in $\text{C}_2\text{H}_4\text{-air}$ mixtures at $T_0=500$ K, $P=100$ torr, and different equivalence ratios. Data points for temperatures measured at the end of the burst (time delay 2 μsec) are circled.

- (a) GRI 3.0 mechanism
- (b) USC / Wang mechanism
- (c) Konnov mechanism

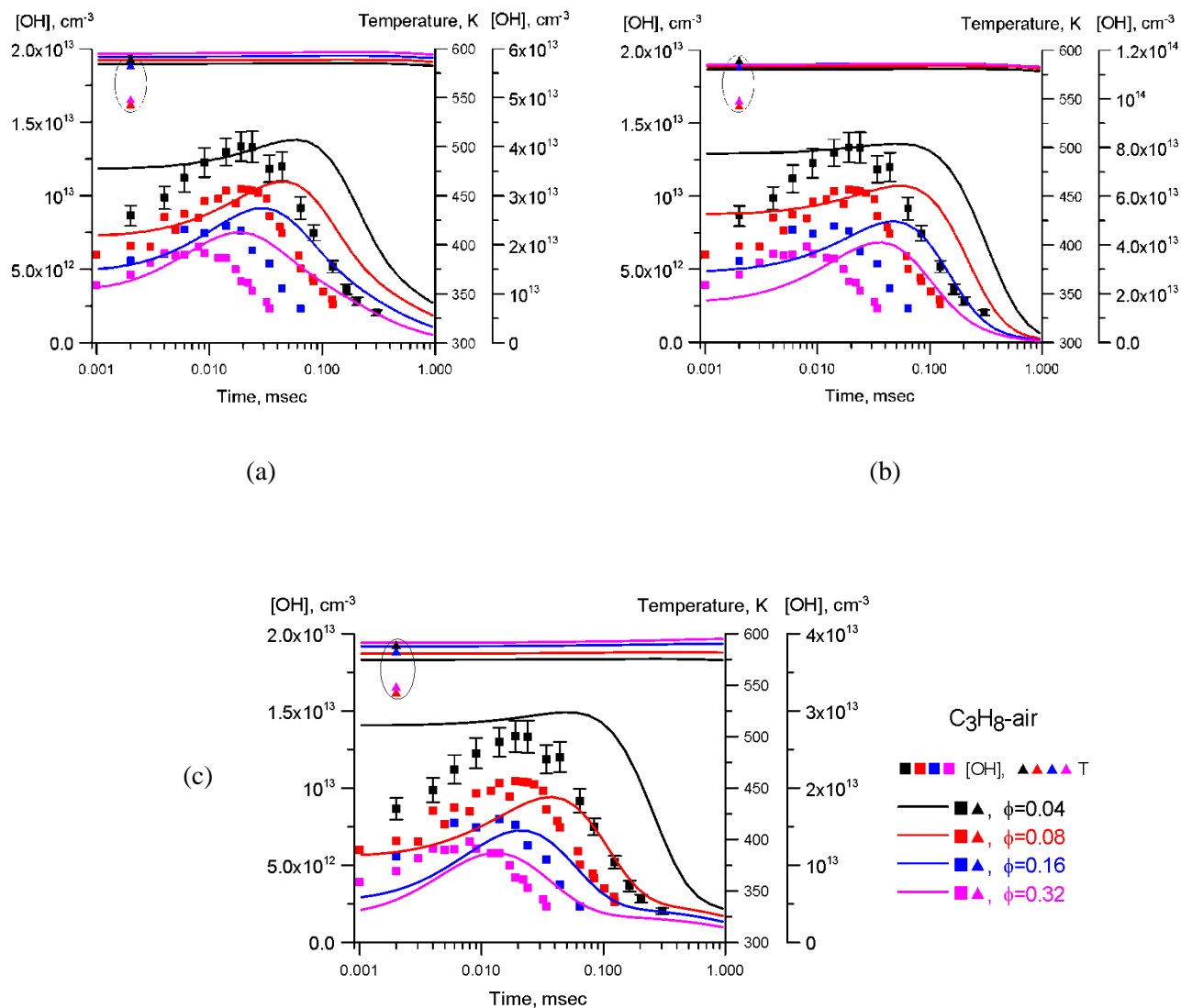


Figure 17: Comparison of experimental and predicted time-resolved, absolute OH number densities after a $\nu=10$ kHz, 50-pulse discharge burst in C_3H_8 -air mixtures at $T_0=500$ K, $P=100$ torr, and different equivalence ratios. Data points for temperatures measured at the end of the burst (time delay 2 μs) are circled.

- (a) GRI 3.0 mechanism
- (b) USC / Wang mechanism
- (c) Konnov mechanism

8. Summary

In the present work, OH Laser Induced Fluorescence (LIF) is used to measure temperature and OH concentration in an atmospheric, near-stoichiometric CH₄-air flame generated by a Hencken burner. OH rotational temperature is inferred both with excitation transitions of the OH A²Σ⁺-X²Π (v'=0, v''=0) band and the (v'=1, v''=0) band. OH LIF signal is corrected by considering transition-dependent total radiative decay rate, fluorescence trapping, and the effect of laser absorption on the overlap integral. The relative OH concentrations are put on an absolute scale by calibrating the optical collection constant using Rayleigh scattering. The absolute OH number density in the flame (with calibration through Rayleigh scattering) is compared with laser absorption measurements done at the same location. Overall, the OH number density calibrated by Rayleigh scattering demonstrates good agreement with absorption measurements both at the center and near the edge of the flame. The OH thermometry values are roughly in accord with values expected for this burner (close to an adiabatic equilibrium value), but it is emphasized that the high OH concentrations that make OH absorption easy to implement also complicate the use of LIF thermometry in particular, requiring the corrections noted above.

Time-resolved absolute OH number density measurements are also performed in fuel-air mixtures in a nanosecond (nsec) pulse discharge cell / plasma flow reactor. Relative OH concentrations are put on an absolute scale by calibrating using Rayleigh scattering. The premixed fuel-air flow in the reactor is excited by a repetitive nsec pulse discharge in a plane-to-plane geometry, operated at a high pulse repetition rate, ν=10 kHz. The experiments are conducted in lean, slowly flowing H₂-air, CH₄-air, C₂H₄-air, and C₃H₈-air mixtures preheated to T₀=500 K in a tube furnace, at a pressure of P=100 torr. In the present measurements, the discharge burst duration is limited to 50 pulses, insufficient to produce plasma-assisted ignition. The discharge uniformity in air and fuel-air flows has been verified using sub-nsec-gated images from an intensified camera demonstrating that diffuse, homogeneous plasma is sustained in the entire range of operating conditions.

The measured, time-resolved, absolute OH number densities demonstrate that OH generated in C₂H₄-air and C₃H₈-air mixtures is highest in very lean mixtures and is reduced by about a factor of 2 as the equivalence ratio is increased by a factor of 8, from φ=0.05 to 0.36 for C₂H₄-air mixture and from φ=0.04 to 0.32 for C₃H₈-air mixture. In these two fuels, transient OH overshoot after the discharge burst, by up to a factor of 2, is detected. No significant overshoot is observed in CH₄-air and in H₂-air mixtures, however. In CH₄-air mixtures, OH concentration is also reduced as the equivalence ratio is reduced, but in H₂-air mixtures, OH concentration after the burst is nearly independent of the equivalence ratio. OH decay rate after the burst in C₂H₄-air and C₃H₈-air occurs on the time scale of ~0.02-0.1 msec, suggesting little accumulation during the burst of pulses. In CH₄-air and H₂-air, the OH decays within ~0.1-1.0 msec and ~0.5-1.0 msec, respectively, suggesting significant OH accumulation in lean mixtures during the burst.

The experimental results are compared with kinetic modeling calculations using a plasma / fuel chemistry model employing several different “conventional” H₂-air and hydrocarbon-air

chemistry mechanisms. Based on this comparison, kinetic mechanisms for H₂-air, CH₄-air, and C₂H₄-air developed by A. Konnov show better overall agreement with the experimental results, compared to H₂-air mechanism developed by Popov, as well as GRI 3.0 and USC / Wang mechanisms. In C₃H₈-air, none of the hydrocarbon chemistry mechanisms tested agrees well with the data. The present results show the need for development of an accurate, predictive low-temperature plasma chemistry / fuel chemistry kinetic model applicable to fuels C₃ and higher.

9. Acknowledgement

This work is supported by the U.S. Air Force Office of Scientific Research MURI “Fundamental Aspects of Plasma Assisted Combustion” (Chiping Li – Technical Monitor).

10. References

- [1] L. Wu, J. Lane, N. P. Cernansky, D. L. Miller, A. A. Fridman and A. Y. Starikovskiy, "Plasma-assisted ignition below self-ignition threshold in methane, ethane, propane and butane-air mixtures," *Proceedings of the Combustion Institute*, vol. 33, pp. 3219-3224, 2011.
- [2] W. Sun, M. Uddi, W. S. H, T. Ombrello, C. Carter and Y. Ju, "Kinetic effects of non-equilibrium plasma-assisted methane oxidation on diffusion flame extinction limits," *Combustion and Flame*, vol. 159, pp. 221-229, 2012.
- [3] W. Kim, M. G. Mungal and M. Cappelli, "The role of in situ reforming in plasma enhanced ultra lean premixed methane/air flames," *Combustion and Flame*, vol. 157, pp. 374-383, 2010.
- [4] Z. Yin, I. V. Adamovich and W. R. Lempert, "OH radical and temperature measurements during ignition of H₂-air mixtures excited by a repetitively pulsed nanosecond discharge," in *accepted for publication in Proceedings of the Combustion Institute*, 2012.
- [5] Y. Zuzeeck, S. Bowman, I. Choi, I. V. Adamovich and W. R. Lempert, "Pure rotational CARS studies of thermal energy release and ignition in nanosecond repetitively pulsed hydrogen-air plasmas," *Proceedings of the Combustion Institute*, vol. 33, pp. 3225-3232, 2011.
- [6] M. Uddi, N. Jiang, I. V. Adamovich and W. R. Lempert, "Nitric oxide density measurements in air and air/fuel nanosecond pulse discharges by laser induced fluorescence," *Journal of Physics D: Applied Physics*, vol. 42, p. 075205, 2009.
- [7] Z. Yin, A. Montello, W. R. Lempert and I. V. Adamovich, "Measurements of temperature and hydroxyl radical generation/decay in lean fuel-air mixtures excited by a repetitively pulsed nanosecond discharge," in *AIAA Plasmadynamics and Lasers Conference*, New Orleans, LA, June 25-28, 2012.
- [8] I. Choi, Z. Yin, I. V. Adamovich and W. R. Lempert, "Hydroxyl radical kinetics in repetitively pulsed hydrogen-air nanosecond plasmas," *IEEE Transactions on Plasma Science*, vol. 39, pp. 3288-

3299, 2011.

- [9] Z. Yin, K. Takashima and I. V. Adamovich, "Ignition time measurements in repetitive nanosecond pulse hydrogen-air plasmas at elevated initial temperatures," *IEEE Transactions on Plasma Science*, vol. 39, pp. 3269-3282, 2011.
- [10] C. Cathey, J. Cain, H. Wang, M. A. Gundersen, C. Carter and M. Ryan, "OH production by transient plasma and mechanism of flame ignition and propagation in quiescent methane-air mixtures," *Combustion and Flame*, vol. 154, pp. 715-727, 2008.
- [11] R. D. Hancock, K. E. Bertagnolli and R. P. Lucht, "Nitrogen and hydrogen CARS temperature measurements in a hydrogen/air flame using a near-adiabatic flat-flame burner," *Combustion and Flame*, vol. 109, pp. 323-331, 1997.
- [12] T. R. Meyer, S. Roy, T. N. Anderson, J. D. Miller, V. R. Katta, R. P. Lucht and J. R. Gord, "Measurements of OH mole fraction and temperature up to 20 kHz by using a diode-laser-based UV absorption sensor," *Applied Optics*, vol. 44, pp. 6729-6740, 2005.
- [13] S. Kostka, S. Roy, P. J. Lakusta, T. R. Meyer, M. W. Renfro, J. R. Gord and R. Branam, "Comparison of line-peak and line-scanning excitation in two-color laser-induced-fluorescence thermometry of OH," *Applied Optics*, vol. 48, pp. 6332-6343, 2009.
- [14] R. P. Lucht, D. W. Sweeney and N. M. Laurendeau, "Laser-saturated fluorescence measurements of OH concentration in flames," *Combustion and Flame*, vol. 50, p. 189, 1983.
- [15] J. Luque and D. R. Crosley, "Absolute CH concentrations in low-pressure flames measured with laser-induced fluorescence," *Applied Physics B*, vol. 63, pp. 91-98, 1996.
- [16] P. Beaud, P. P. Radi, H. -M. Franzke, B. Mischler, T. A. -P and T. Gerber, "Picosecond investigation of the collisional deactivation of OH $A^2\Sigma^+(v'=1, N'=4, 12)$ in an atmospheric-pressure flame," *Applied Optics*, vol. 37, p. 3354, 1998.
- [17] G. Herzberg, *Molecular Spectra and Molecular Structure: I. Spectra of Diatomic Molecules*, New York: Van Nostrand Reinhold, 1950.
- [18] J. A. Coxon, "Optimum molecular constants and term values for the $X^2\Pi(v\leq 5)$ and $A^2\Sigma^+(v\leq 3)$ states of OH," *Canadian Journal of Physics*, vol. 58, p. 933, 1980.
- [19] J. Luque and D. R. Crosley, "LIFBASE, database and spectral simulation for diatomic molecules," SRI International Report MP-99-009, 1999.
- [20] E. C. Rea, A. Y. Chang and R. K. Hanson, "Shock-tube study of pressure broadening of the $A^2\Sigma^+-X^2\Pi(0,0)$ band of OH by Ar and N_2 ," *Journal of Quantitative Spectroscopy and Radiative Transfer*, vol. 37, pp. 117-127, 1987.

- [21] E. C. Rea, A. Y. Chang and R. K. Hanson, "Collisional broadening of the $A^2\Sigma^+-X^2\Pi$ (0,0) band of OH by H_2O and CO_2 in atmospheric-pressure flames," *Journal of Quantitative Spectroscopy and Radiative Transfer*, vol. 41, pp. 29-42, 1989.
- [22] P. H. Paul, "Vibrational energy transfer and quenching of OH $A^2\Sigma^+(v'=1)$ measured at high temperatures in a shock tube," *Journal of Physical Chemistry*, vol. 99, p. 8472, 1995.
- [23] A. Bucholtz, "Rayleigh scattering calculations for the terrestrial atmosphere," *Applied Optics*, vol. 34, pp. 2765-2773, 1995.
- [24] D. R. Bates, "Rayleigh scattering by air," *Planetary Space Science*, vol. 32, pp. 785-790, 1984.
- [25] A. Montello, Z. Yin, D. Burnette, I. V. Adamovich and W. R. Lempert, "Picosecond CARS measurements of nitrogen vibrational loading and rotational/translational temperature in non-equilibrium discharges," in *43rd AIAA Plasmadynamics and Laser Conference*, New Orleans, LA, June 25-28, 2012.
- [26] M. Uddi, N. Jiang, E. Mintusov, I. V. Adamovich and W. R. Lempert, "Atomic oxygen measurements in air and air/fuel nanosecond pulse discharges by two photon laser induced fluorescence," *Proceedings of the Combustion Institute*, vol. 32, pp. 929-936, 2009.
- [27] I. A. Kossyi, A. Y. Kostinsky, A. A. Matveyev and V. P. Silakov, "Kinetic scheme of the nonequilibrium discharge in nitrogen-oxygen mixture," *Plasma Source Science and Technology*, vol. 1, pp. 207-220, 1992.
- [28] N. A. Popov, "Effect of a pulsed high-current discharge on hydrogen-air mixtures," *Plasma Physics Report*, vol. 34, pp. 376-391, 2008.
- [29] N. Moreau, S. Pasquiers, N. Blin-Simiand, L. Magne, F. Jorand, C. Postel and J. -R. Vacher, "Propane dissociation in a non-thermal high-pressure nitrogen plasma," *Journal of Physics D: Applied Physics*, vol. 43, p. 285201, 2010.
- [30] A. Konnov, "Remaining uncertainties in the kinetic mechanism of hydrogen combustion," *Combustion and Flame*, vol. 152, pp. 507-528, 2008.
- [31] "GRI-Mech 3.0," http://www.me.berkeley.edu/gri_mech/version30/text30.html.
- [32] H. Wang, X. You, A. V. Joshi, S. G. Davis, A. Laskin, F. Egolfopoulos and C. K. Law, "USC Mech Version II. High-Temperature Combustion Reaction Model of $H_2/CO/C_1-C_4$ Compounds," http://ignis.usc.edu/USC_Mech_II.htm.
- [33] A. Konnov, "Detailed reaction mechanism for small hydrocarbons combustion, Release 0.5," 2000. <http://homepages.vub.ac.be/~akonnov/>.

- [34] R. Atkinson, D. L. Baulch, R. A. Cox, J. N. Crowley, R. F. Hampson, R. G. Hynes, M. E. Jenkin, M. J. Rossi and J. Troe, "Evaluated kinetic and photochemical data for atmospheric chemistry: Volume I - gas phase reactions of O_x, HO_x, NO_x, and SO_x species," *Atmospheric Chemical Physics*, vol. 4, pp. 1461-1738, 2004.